

Cite this: *Chem. Sci.*, 2025, 16, 21298

Spin chemistry: the key to revolutionizing energy storage and conversion efficiency

Xiaolin Zhang,^{†a} Jinhao Pan,^{†a} Yi Wan,[ⓑ] Xueqing Zheng,^a Yutong Liu,^a Yan Zhang,^a Xingyu Liu,^a Qi Wei,^a Jiashuo Wu,^a Pawin lamprasertkun,^{ⓑc} Bin Wang,^{ⓑ*a} Mingbo Wu^{ⓑab} and Han Hu^{ⓑ*a}

As a fundamental property of electrons, spin and its interactions profoundly influence chemical processes and material properties. In this review, we focus on key advances in spin chemistry for energy storage and conversion technologies. Starting from the basic concepts of spin and theoretical computations, we discuss its role in the mechanisms of electrochemical thermodynamics and kinetics. We then examine advanced characterization techniques, particularly emerging *in situ* electrochemical methods, and summarize how these have led to new insights into electrochemical mechanisms mediated by spin effects. Next, we review the applications of spin manipulation in electrocatalysis and energy storage, along with strategies for performance enhancement and regulation, with emphasis on the intrinsic interrelationships between catalysis and energy storage systems. Finally, we outline future perspectives for spin chemistry in energy conversion and storage, particularly in the context of big data and artificial intelligence, which are poised to enhance mechanistic understanding, accelerate materials design, and improve the interpretation of structure–activity relationships. This interdisciplinary integration not only accelerates the development of sustainable, high-performance energy technologies but also lays a foundation for future innovations in spin-driven materials science.

Received 31st August 2025
Accepted 27th October 2025

DOI: 10.1039/d5sc06699a

rsc.li/chemical-science

1 Introduction

The rapid pace of global industrialization and continuous population growth are driving an exponential surge in energy demand. However, our heavy reliance on fossil fuels is not only depleting resources faster but also causing severe environmental crises.¹ These include worsening global warming from greenhouse gas emissions, more frequent extreme weather events, and disruption to ecosystems. To address these challenges, there is now a strong global push towards carbon neutrality by transforming our energy systems, aiming for truly sustainable development. Renewable energy sources like solar, wind, and hydropower offer promising alternatives to fossil fuels because they are clean and sustainable. But their inherent intermittency and instability make large-scale deployment difficult. We urgently need efficient energy storage and conversion (ESC) technologies to bridge the gap between

fluctuating power generation and the steady demand of end users. ESC systems play a crucial role here. They convert variable electricity into storable chemical fuels like hydrogen or methanol, or deliver electricity directly to the grid. This helps create integrated “generation-storage-utilization” energy networks.²

Electrocatalysis sits at the heart of energy conversion. It drives critical reactions such as hydrogen evolution (HER)³ and oxygen evolution (OER)⁴ in water splitting, carbon dioxide reduction (CO₂RR),⁵ and oxygen reduction (ORR)⁶ in fuel cells. By controlling how electrons move at interfaces, this technology directly turns renewable electricity into high energy density green fuels or enables efficient power generation. For example, water electrolysis stores surplus energy as hydrogen, while fuel cells convert that hydrogen back into electricity, forming a potential “hydrogen economy” loop. However, the efficiency and scalability of these processes depend on catalyst performance. Precious metal catalysts (Pt, Ru, Ir *et al.*) show excellent activity but face major hurdles for widespread use because they are scarce and extremely expensive.⁷ In contrast, non-precious alternatives often suffer from lower activity or poor durability. Developing catalysts that are highly active, long-lasting, and cost-effective remains a critical challenge for advancing electrocatalytic technologies. Alongside electrocatalysis, innovations in energy storage systems, including lithium-ion batteries (LIBs), supercapacitors and emerging metal–air

^aState Key Laboratory of Heavy Oil Processing, Shandong Key Laboratory of Advanced Electrochemical Energy Storage Technologies, College of Chemistry and Chemical Engineering, College of New Energy, China University of Petroleum (East China), Qingdao 266580, P. R. China. E-mail: bin.wang@upc.edu.cn; hhu@upc.edu.cn

^bCollege of Chemical Engineering, Qingdao University of Science & Technology, Qingdao 266061, P. R. China

^cSchool of Bio-Chemical Engineering and Technology, Sirindhorn International Institute of Technology, Thammasat University, Pathum Thani 12120, Thailand

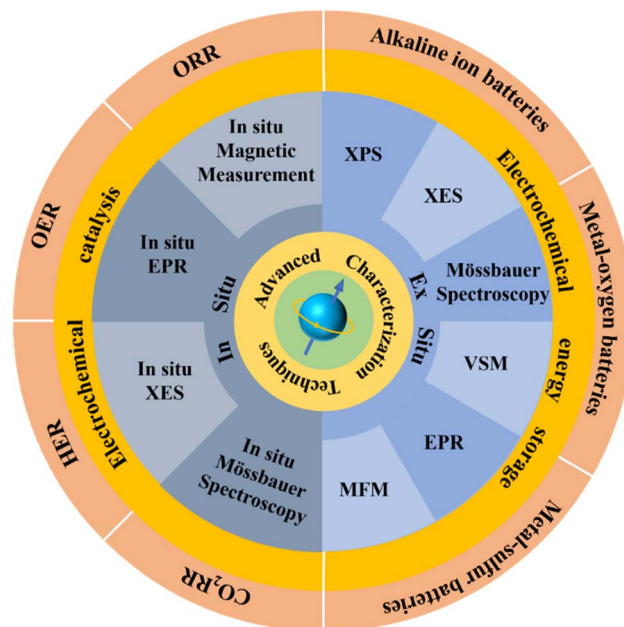
[†] Z. XL and P. JH contributed equally.



batteries, demand breakthroughs in materials science. Persistent issues with energy density, cycle life, and safety often stem from limitations in electrode materials and the dynamics of reactions at interfaces. For instance, the “shuttling” of polysulfides in lithium–sulfur (Li–S) batteries and high resistance at interfaces in solid-state batteries highlight the urgent need for novel material designs. Tackling these key challenges requires control over electrons at the atomic scale.⁸

Electron spin is a fundamental quantum mechanical property. Unlike classical particles, electrons possess an intrinsic angular momentum independent of their movement through space.⁹ Wolfgang Pauli introduced the concept of spin in 1925 to explain anomalies in atomic spectra. Dirac's later relativistic quantum theory provided the mathematical framework, confirming its quantized nature: electrons exist in discrete “spin-up” or “spin-down” states defined by quantum numbers. Spin underpins core principles like the Pauli exclusion principle and Hund's rules, which dictate how electrons behave in atoms and molecules.^{10–12} The landmark Stern–Gerlach experiment (1922) directly demonstrated spin quantization, showing silver atoms splitting into distinct paths in a magnetic field, a cornerstone of quantum theory. Beyond atomic-scale magnetism, spin governs phenomena like the Zeeman effect and influences material properties such as conductivity and magnetic ordering through spin polarization. This occurs when an external field or material-specific interactions cause an imbalance between the number of “spin-up” and “spin-down” electrons. Spin dynamics represent a critical, yet largely unexplored, avenue for boosting efficiency in electrochemical systems.^{13–15} Transition metal catalysts exploit changes in spin state, for instance, putting Fe or Co centers into a high-spin (HS) configuration to adjust how their orbitals interact with reactant molecules. This can directly lower the energy barrier for reactions like oxygen evolution or reduction.¹⁶ At electrode interfaces, spin polarization can optimize charge transfer by aligning electron spins, reducing scattering losses and improving conductivity. The Chirality-Induced Spin Selectivity (CISS) effect is a prime example, where chiral molecules selectively transmit electrons based on their spin, enhancing energy conversion efficiency without needing an external magnet.¹⁷ In energy storage, spin transitions in materials like Mn³⁺/Mn⁴⁺ or Co²⁺/Co³⁺ affect crystal lattice stability and how easily ions can move. Spin-aligned pathways in systems like Li–S batteries could also help suppress the problematic polysulfide shuttle effect. Advanced techniques like electron paramagnetic resonance allow us to probe spin densities, linking microscopic behavior to overall device performance. Despite progress, significant challenges remain. These include untangling the complex effects of spin–orbit coupling (SOC) in catalysts containing heavy elements and designing practical, scalable interfaces that exploit spin selectivity. These challenges position spin manipulation as a key frontier for next-generation breakthroughs in electrochemistry.¹⁸

The rapid advancement and growing interest in spin-related electrochemistry have led to a surge in studies integrating spin phenomena with electrochemical systems, as well as a proliferation of reviews in this interdisciplinary area.¹⁹ However, most



Scheme 1 The schematic of the characterization and application of electronic spin polarization.

existing reviews focus either on catalysis or energy storage, overlooking the critical interdependencies between the two. Extensive evidence indicates that catalytic processes play an indispensable role in energy storage systems.^{20,21} In this review, we establish a “spin-energy” framework to systematically elucidate how spin effects operate synergistically across both energy conversion and storage processes. We examine the universal influence of spin on key steps such as charge transfer kinetics, the binding behavior of reaction intermediates at surfaces, and reaction pathways. Furthermore, we provide a detailed discussion of advanced techniques for characterizing spin properties, along with recent applications of spin manipulation in electrocatalysis and energy storage, including various strategies for spin regulation. We also summarize the latest advances in artificial intelligence applied to spin chemistry from limited reported literature, while offering an in-depth discussion of the future prospects of AI-driven developments in electrochemical spin research. Ultimately, this review aims to accelerate the translation of spin control strategies from theoretical concepts into high-efficiency, durable energy systems, thereby advancing sustainable energy solutions (Scheme 1).

2 Fundamental mechanisms of spin–electrochemical coupling

Electron spin is an intrinsic angular momentum of electrons, described in quantum mechanics as a non-classical inherent property with a quantum number $S = \frac{1}{2}$. The corresponding spin magnetic moment is expressed as:

$$\mu_s = -g_s \mu_B \sqrt{s(s+1)} \quad (1)$$





Fig. 1 Spin alignment of electrons in a magnetic field due to the Zeeman interaction. Reproduced with permission.² Copyright 2023, the Royal Society of Chemistry.

where $g_s \approx 2$ is the electron spin g -factor, and $\mu_B = \frac{e\hbar}{2m_e}$ is the Bohr magneton.²² According to the Pauli exclusion principle, two electrons in the same atomic orbital must have opposite spin orientations ($m_s = +\frac{1}{2}$ and $m_s = -\frac{1}{2}$), a constraint that directly governs electron configurations in atoms/molecules and chemical bond formation. In an external magnetic field (B), the interaction energy between electron spin and the field is described by the Zeeman effect:

$$E = -\mu_s \cdot B = g_s \mu_B m_s B \quad (2)$$

This energy difference induces spin-state splitting (spin-up vs. spin-down) and triggers spin polarization, a phenomenon where a specific spin orientation dominates within an electron population. The quantum nature of spin not only governs material magnetism (*e.g.*, ferromagnetic and antiferromagnetic ordering) but also influences electronic band structures and dynamical behaviors through SOC. The Hamiltonian form of SOC is:

$$H_{\text{SOC}} = \lambda L \cdot S \quad (3)$$

where λ is the coupling constant, L and S are the orbital and spin angular momentum operators, respectively. This interaction is particularly significant in transition metal catalysts, where it modulates the spin states of d -orbital electrons (*e.g.*, high spin vs. low spin configurations), thereby altering the adsorption strength of reaction intermediates and activation energy barriers. In summary, the quantum mechanical essence of electron spin and its coupling with external fields (magnetic or crystal fields) provide a critical theoretical foundation for understanding macroscopic material properties and microscopic dynamics.^{23,24} The following section will systematically elaborate on the thermodynamic (*e.g.*, spin polarization effects on charge transfer free energy) and kinetic (*e.g.*, spin selective electron transfer rates) roles of spin in energy storage systems (*e.g.*, LIBs) and electrocatalytic processes (*e.g.*, OER/ORR).⁷

Electron spin, as a fundamental quantum degree of freedom, transcends its traditional role in governing magnetic properties to emerge as a critical regulator in electrochemical processes.⁹ The core of spin–electrochemical coupling lies in spin-dependent charge transfer across electrode–electrolyte interfaces. Unlike conventional models that treat electrons as mere spin-less charges, we emphasize that the spin state of electrons directly influences their tunneling probability, the adsorption configuration of intermediates, and ultimately, reaction kinetics and selectivity.¹²

The rate of electron transfer in electrochemical reactions is not solely determined by overpotential but is intrinsically spin-sensitive. This sensitivity stems from two primary quantum phenomena: spin selection rules and spin-polarized tunneling.²² According to spin selection rules, electron transfer between species with specific spin states, such as from a singlet-state catalyst to a triplet-state oxygen molecule, must obey spin conservation. Spin-forbidden reactions face significantly higher activation barriers, though spin–orbit coupling can modulate these barriers by enabling spin-flip processes, thereby opening

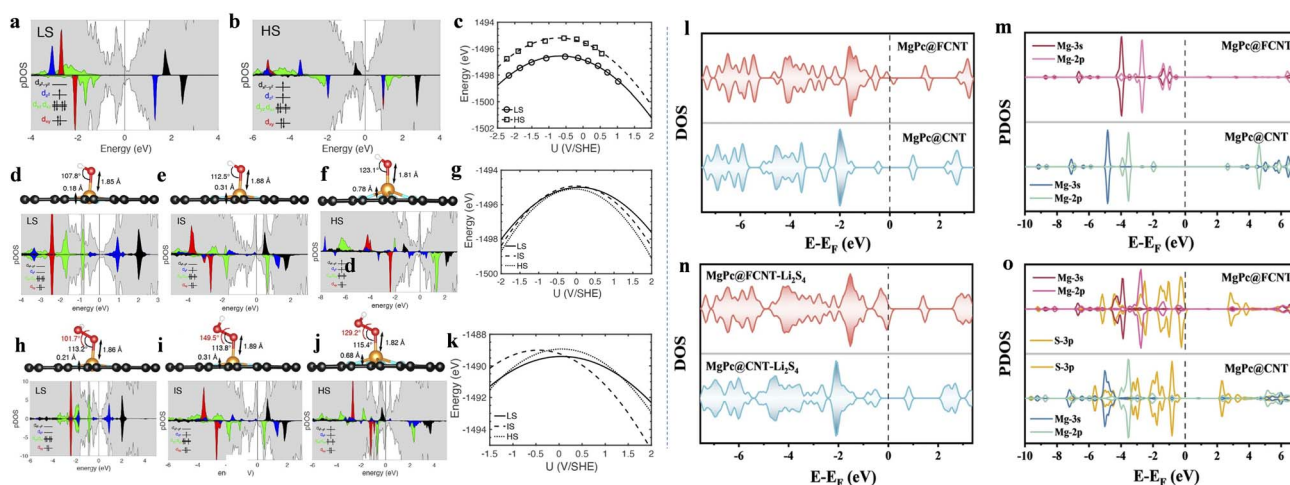


Fig. 2 Projected density of states (pDOS) of the 3d orbitals of Co ions, atomic structures, and the potential-dependent total energies with polynomial fits for the LS and HS states of CoN_4 (a–c); for the LS, intermediate-spin (IS), and HS states of $^*\text{OH}/\text{CoN}_4$ (d–g); and for the LS, IS, and HS states of $^*\text{O}_2\text{H}/\text{CoN}_4$ (h–k). Copyright 2020, American Chemical Society.³⁴ Electronic structure evolution of $\text{MgPc}@/\text{FCNT}$ and $\text{MgPc}@/\text{CNT}$ systems upon Li_2S_4 adsorption: (l and n) calculated total DOS before and after adsorption, respectively; (m and o) projected DOS (PDOS) of the Mg 3s and 2p orbitals before and after adsorption. Copyright 2024, Springer Nature.³⁷



otherwise inaccessible reaction pathways.²³ This is particularly crucial in electrocatalytic reactions like the ORR, where the triplet ground state of O₂ presents a fundamental kinetic challenge. Meanwhile, spin-polarized tunneling describes how the probability of an electron tunneling through an energy barrier depends on its spin orientation when the electrode or adsorbate exhibits spin polarization. Ferromagnetic electrodes inject spin-polarized currents, in which one spin channel may experience lower interfacial resistance than the other, leading to spin-selective electrocatalysis.⁶ A distinctive feature of electrochemical systems is the ability to tune the Fermi level *via* applied electrode potential, offering a powerful *in situ* means to manipulate spin interactions. In transition metal catalysts, the energy difference between HS and low spin (LS) states is often comparable to thermal energy.¹⁶ Variations in the applied potential can shift the Fermi level, altering the occupancy of frontier d-orbitals and thereby inducing spin-state transitions that optimize intermediate binding. Moreover, the degree of spin polarization at the Fermi level, which governs the efficiency of spin-polarized electron transfer, is itself a function of electrode potential. This creates a feedback mechanism wherein the potential not only drives the reaction but also dynamically tunes the spin character of active sites. The magnetic ordering of a catalyst—whether ferromagnetic, antiferromagnetic, or paramagnetic, governs the electronic structure at the surface and thereby influences the adsorption energy of reaction intermediates. The interaction between spin-polarized d-bands of a magnetic catalyst and the molecular orbitals of an adsorbate is spin-sensitive. For instance, in the OER, the adsorption strength of *OH or *O species can vary considerably with different surface spin configurations, directly affecting the catalytic overpotential.^{6,7} Furthermore, ferromagnetic ordering promotes long-range electron delocalization, enhancing electrical conductivity and enabling efficient charge compensation during adsorption and desorption, a phenomenon that is less pronounced in spin-disordered systems (Fig. 1 and 2).

2.1 Thermodynamic and kinetic of spin effects in energy storage systems

The dynamic aspects of spin-related phenomena focus on the temporal evolution and rate-governed processes in energy storage systems. Central to this is SP, which modulates the efficiency of charge transport within battery electrodes by influencing the alignment of electron spins under magnetic fields. For instance, in LIBs, SP alters the kinetics of ion intercalation at electrode–electrolyte interfaces through selective occupation of spin-dependent electronic states, thereby accelerating Li⁺ migration and redox reactions.^{25,26} Similarly, in redox flow batteries, SP enhances the reaction rates of electroactive species by optimizing spin-aligned electron transfer pathways, directly improving charge–discharge efficiency. A critical mechanism involves spin-magnetic field interactions, where phase shifts between spin states induce directional polarization, dynamically modifying material reactivity. This control over reaction pathways enables the suppression of parasitic side reactions, such as electrolyte decomposition, by steering

electron transfer toward desired channels. Furthermore, spin manipulation strategies allow precise tuning of electrochemical kinetics, including ion diffusion barriers and interfacial charge transfer resistance, which collectively govern battery performance metrics like charging speed and cycle durability. The experimental complexity lies in real-time monitoring of spin dynamics, requiring advanced spectroscopic techniques to resolve transient spin states during operational conditions.²⁷

Thermodynamically, spin effects are governed by energy landscapes and equilibrium states in magnetic materials. The energy disparity between spin-up and spin-down electrons in magnetic fields dictates their population distribution, as described by spin-dependent density of states. Ferromagnetic materials exhibit spontaneous spin alignment below the Curie temperature, maintaining a stable magnetization without external energy input a metastable thermodynamic state. Conversely, antiferromagnetic systems achieve energy minimization through antiparallel spin arrangements, nullifying macroscopic magnetization until thermal fluctuations above the Néel temperature disrupt this order. Paramagnetic substances, with randomly oriented spins at equilibrium, transiently align under external fields but revert to disorder upon field removal, reflecting entropy-driven equilibrium restoration. SP interfaces with thermodynamics by altering activation energies of electrochemical processes; for example, spin-polarized charge carriers reduce the thermodynamic driving force for detrimental side reactions, stabilizing electrode materials. Temperature-dependent spin behavior further links thermal energy to magnetic phase transitions critical for designing batteries operating across temperature ranges. The thermodynamic stability of spin configurations also impacts long-term material degradation, as misaligned spins may induce lattice strain or electronic instability. Ultimately, the interplay between spin-derived energy states and thermal equilibrium governs the feasibility of spin-engineered materials for high-efficiency, durable energy storage systems.²⁸

2.2 Thermodynamic and kinetic of spin effects in electrocatalytic

The thermodynamic framework governing catalytic processes is fundamentally shaped by energy equilibria and spin-mediated interactions. A critical parameter is the reaction enthalpy (ΔH), which is modulated by spin-related phenomena such as spin–orbital coupling. These interactions reconfigure the electronic structure of catalytic active sites, reducing coulombic repulsion between reactants (*e.g.*, triplet-state oxygen) and the catalyst surface. This adjustment lowers energy barriers for electron transfer, as quantified by:

$$\Delta H = \Delta H_0 - \Delta H_{\text{spin}} \quad (4)$$

where ΔH_{spin} represents spin-dependent enthalpy shifts. Concurrently, entropy (ΔS) plays a pivotal role, dictated by the spin degeneracy (g_{spin}) and configurational states ($g_{C_e^-}$) of electrons. Ferromagnetic catalysts exhibit ordered spin alignment ($g_{\text{spin}} = 1$), yielding negligible entropy loss ($\Delta S_{e^-} \approx 0$), whereas paramagnetic systems ($g_{\text{spin}} = 2$) suffer entropy



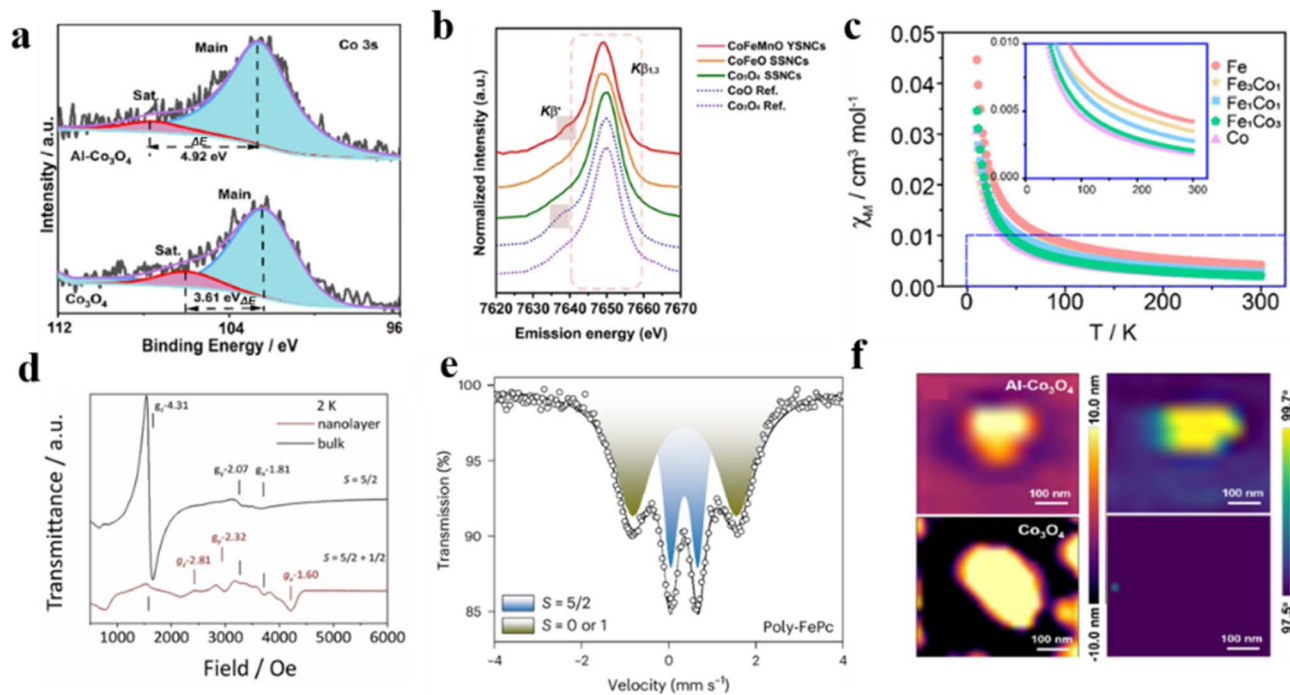


Fig. 3 (a) Co 3s XPS spectra of Co_3O_4 with and without Al doping. Reproduced with permission.³⁹ Copyright 2024, Wiley-VCH. (b) Co $K\beta$ XES spectra of CoFeMnO YSNs, CoFeO SSNCs, Co_3O_4 SSNCs, CoO ref. and Co_3O_4 ref. Reproduced with permission.⁴⁹ Copyright 2024, Wiley-VCH. (c) Magnetic susceptibility of TM-DABDT with various Fe/Co ratios. Reproduced with permission.⁶⁰ Copyright 2023, Wiley-VCH. (d) X-band EPR for bulk and nanolayer samples at 2 K. Reproduced with permission.⁷⁵ Copyright 2024, Wiley-VCH. (e) Mössbauer spectra of Poly FePc. Reproduced with permission.⁵⁴ Copyright 2025, Nature Publishing Group. (f) The AFM topographical (left) and MFM (right) image of the Co_3O_4 and Al- Co_3O_4 samples. Reproduced with permission.³⁹ Copyright 2024, Wiley-VCH.

doping induced optimization of the Ni–O–Mn super-exchange pathway, facilitated by the dopant's pronounced electronegativity and compact ionic radius. This dual modulation effect simultaneously promotes transition of Ni ions to a HS configuration while stabilizing Mn ions in their LS state.

3.1.3 Vibrating sample magnetometer (VSM). Variable-temperature magnetic susceptibility measurements can directly quantify the number of unpaired electrons. By analyzing the temperature-dependent magnetic susceptibility curve (χ - T), the effective magnetic moment (μ_{eff}) can be determined. This moment relates to the number of unpaired electrons (n) through the following equation:⁵¹

$$\mu_{\text{eff}} = \sqrt{n(n+1)}\mu_{\text{B}} \quad (5)$$

Different spin states can be further quantified and their relative fractions in the material evaluated using this relationship, thereby enabling assessment of qualitative spin-state manipulation strategies:

$$\mu_{\text{eff}} = \sqrt{8C}\mu_{\text{B}} \quad (6)$$

$$\mu_{\text{eff}} =$$

$$g\mu_{\text{B}}\sqrt{S_{\text{HS}}(S_{\text{HS}}+1)V_{\text{HS}}+S_{\text{MS}}(S_{\text{MS}}+1)V_{\text{MS}}+S_{\text{LS}}(S_{\text{LS}}+1)V_{\text{LS}}} \quad (7)$$

$$V_{\text{HS}} + V_{\text{MS}} + V_{\text{LS}} = 1 \quad (8)$$

In the aforementioned equations, C is the Curie constant, determined by fitting the magnetic susceptibility ($\chi = M/H$) above the paramagnetic transition temperature. It obeys the Curie–Weiss law $\chi = C/(T - \theta)$, where θ denotes the Curie–Weiss temperature. g is the Lande factor ($g = 2$), while S_{HS} , S_{MS} , and S_{LS} are the spin quantum number (S) of HS, mediate spin (MS) and LS state, respectively. For example, in Fe^{3+} , $S_{\text{HS}} (=5/2)$, $S_{\text{MS}} (=3/2)$, and $S_{\text{LS}} (=1/2)$. V_{HS} , V_{MS} , and V_{LS} are the volume fraction for metal ions in HS, MS, and LS states, respectively.⁵²

For example, calculations based on χ - T curves using Langevin theory reveal significant differences in the effective magnetic moments of differently doped transition metal ion coordination compounds, such as Fe-DABDT and Co-DABDT (where DABDT = 2,5-diaminobenzene-1,4-dithiol).⁵³ The moments are $3.14 \mu_{\text{B}}$ for Fe-DABDT and $2.08 \mu_{\text{B}}$ for Co-DABDT, respectively. Furthermore, the number of unpaired electrons (using eqn (1)) differs by over two-fold (3 for Fe-DABDT vs. 1.31 for Co-DABDT). This disparity primarily originates from the nucleophilic reaction enabled by the magnetized Fe sites, which accelerates the polarization of electron spin states. Building on this foundation, the percentage distribution of different spin states within the system can be further calculated. Taking the FeN_4 model as an example: coordination with adjacent graphitic nitrogen increases the μ_{eff} from an initial value of $2.16 \mu_{\text{B}}$ (sample named as Fe- N_4) to $5.82 \mu_{\text{B}}$ (sample named as Fe-



N_4 /NGC-C), and the number of unpaired electrons rises from 1.4 to 4.8. Subsequent calculations (eqn (2)–(4)) reveal that the proportion of HS surges from an initial 5.2% to 96.6% after coordination with adjacent graphitic nitrogen (Fe– N_4 /NGC-C).⁵¹ This computational approach is applicable not only to single metal ion systems but also to mixed metal ion systems, as demonstrated by Du *et al.*⁵³

3.1.4 Electron paramagnetic resonance (EPR). EPR spectroscopy probes spin states of transition metal ions by diagnosing g value anomalies, zero-field splitting (ZFS) effects, and signal detectability patterns, where HS species typically display broad resonances at high g values (*e.g.*, $g = 6.0$ for HS Fe^{3+} ($S = 5/2$))⁵⁴ or characteristic splitting (*e.g.*, six-line hyperfine structure at $g = 2.0$ for HS ($S = 5/2$) Mn^{2+}),⁵⁵ while LS ions exhibit sharp signals near $g = 2.0$ (exemplified by LS ($S = 1/2$) Fe^{3+} in cytochrome *c* with $g = [2.4, 2.2, 1.9]$),⁵⁶ crucially, LS Co^{3+} ($S = 0$) remains EPR silent⁵⁷ whereas HS Co^{2+} ($S = 3/2$) shows anisotropic signals at $g \approx 6.0$ in hydrated complexes,⁵⁸ though detection often requires cryogenic temperatures to resolve ZFS-broadened features in HS ions like Mn^{3+} ($S = 2$, $g \approx 4.8$ in oxygen evolving complexes).⁵⁹ For instance, the mechanical exfoliation of the metal-organic layer induces partial spin crossover at the Fe^{3+} centers. As revealed by the X-band EPR spectra at 2 K, the exfoliated nanolayers exhibit additional LS signals at $g_x = 1.60$, $g_y = 2.32$ and $g_z = 2.81$ alongside the original peaks ($g_x = 1.81$, $g_y = 2.07$ and $g_z = 4.31$) observed in the bulk sample, confirming the occurrence of spin crossover (Fig. 3c and d).⁶⁰ Inspired by natural systems, Zhang *et al.* constructed dual $\equiv Fe^{II} \cdots Fe^{II} \equiv$ sites by selectively removing bridging sulfur atoms from pyrite (FeS_2). Subsequent room-temperature oxidation during which a superoxide radical intermediate is generated, enabled the synthesis of HS ($S = 2$) $Fe^{IV}=\text{O}$, a highly reactive intermediate that accelerates methane oxidation to methanol. To verify the successful formation of the HS $Fe^{IV}=\text{O}$ species, low-temperature (77 K) EPR spectroscopy was employed. The spectrum exhibited anisotropic signals with g -values of $g_1 = 2.011$, $g_2 = 2.002$, and $g_3 = 1.997$, indicating the generation of a superoxide radical intermediate and confirming the efficacy of the room-temperature oxidation process. Furthermore, the presence of significant ZFS provided additional evidence for the formation of HS ($S = 2$) $Fe^{IV}=\text{O}$.⁶¹

In addition, characterizing HS metal ions requires cryogenic temperatures (2–77 K) to suppress relaxation-induced broadening, while high concentrations induce spin-spin coupling that broadens spectral lines, which is the particular challenge for solid-state samples.⁶² Although EPR qualitatively distinguishes spin states, it cannot directly quantify relative populations; mixed-spin systems (*e.g.*, Fe^{2+}/Fe^{3+}) thus require validation *via* complementary techniques like Mössbauer spectroscopy. Consequently, EPR should be integrated with magnetometry, XAS, or other methods to prevent misinterpretations. For complex systems, multi-frequency EPR (X/Q/W-band) is recommended to resolve anisotropic signatures.

3.1.5 Mössbauer spectroscopy. Mössbauer spectroscopy deciphers transition metal spin states by analyzing isomer shift (δ) variations, quadrupole splitting (ΔEQ), and magnetic

hyperfine splitting patterns, where HS states exhibit larger δ and ΔEQ values than LS counterparts due to elongated metal-ligand bonds and symmetry breaking. This is exemplified by HS Fe^{2+} ($Fe_3Al_2Si_3O_{12}$: $\delta \approx 1.2\text{--}1.3 \text{ mm s}^{-1}$, $\Delta EQ \approx 3.4\text{--}3.6 \text{ mm s}^{-1}$)⁶³ *vs.* LS Fe^{3+} (Prussian white: $\delta \approx -0.1 \text{ mm s}^{-1}$, $\Delta EQ \approx 0$),⁶³ while Co systems show contrasting HS Co^{2+} (CoO: $\delta \approx +0.5 \text{ mm s}^{-1}$, $\Delta EQ \approx 4.1 \text{ mm s}^{-1}$)⁶⁴ and LS Co^{3+} ($K_3[Co(CN)_6]$: $\delta \approx -0.8 \text{ mm s}^{-1}$, $\Delta EQ \approx 0.3 \text{ mm s}^{-1}$).⁶⁴ For Mn, HS Mn^{3+} (Mn_2O_3 : $\delta \approx +0.35 \text{ mm s}^{-1}$, $\Delta EQ \approx 2.8 \text{ mm s}^{-1}$)⁶⁵ displays J-T-distorted signatures absent in LS states, though ⁵⁵Mn/⁵⁹Co measurements require cryogenic conditions or magnetic fields to resolve spin-crossover dynamics (*e.g.*, δ shift from 1.1 to 0.3 mm s^{-1} in Phenanthroline complexes during HS to LS transition).⁶³ Despite 100% natural abundance of ⁵⁹Co and ⁵⁵Mn isotopes, Mössbauer spectroscopy for Co/Mn systems exhibits lower resolution than ⁵⁷Fe due to higher γ -ray energies. Quantitative analysis necessitates spectral deconvolution using fitting software (*e.g.*, MossWinn) coupled with crystal field theory calculations. While this technique is indispensable for iron-based materials, its application to Co/Mn systems requires integration with XANES and magnetic measurements to mitigate misinterpretation risks.⁷⁰

For example, Ni doping was performed on perovskite oxide fuel electrode materials to obtain $Sr_2Fe_{1.3}Ni_{0.2}Mo_{0.5}O_6$ (SFNM).⁷¹ Mössbauer spectroscopy found that the singlet state representing HS Fe^{4+} increased from 22.7% to 40.4%, while the doublet state content representing HS Fe^{3+} decreased from 77.3% to 59.6%. This change is mainly caused by the double exchange effect coupling generated by Ni after doping. In addition, to analyze the spin state of the active center Fe in Fe–N–C catalysts, Mössbauer spectroscopy was used to test several types of Fe–N–C catalysts (Fig. 3e).⁵⁴ It was found that high-purity FePc and FePc–FePc samples showed a single characteristic peak in the Mössbauer spectrum, with $\Delta EQ = 1.28 \text{ mm s}^{-1}$ and $\delta = 0.32 \text{ mm s}^{-1}$. Combined with EPR ($g = 4.0$), the spin quantum number of the active center Fe was determined to be $S = 3/2$. The poly-FePc sample, however, showed two spin states: the main component with $\Delta EQ = 2.31 \text{ mm s}^{-1}$, attributed to the $Fe^{2+}N_4$ structure without ligand binding, accounting for 65%; and the secondary component with $\Delta EQ = 0.63 \text{ mm s}^{-1}$, corresponding to the $OH-Fe^{3+}N_4$ ($S = 5/2$) structure, accounting for 35%. This provides significant theoretical support for further optimizing the catalytic performance of Fe–N–C catalysts.

3.1.6 Magnetic force microscopy (MFM). MFM is developed based on Atomic Force Microscopy (AFM). It can detect the magnetic field intensity on the material surface with extremely high resolution, reaching the nanoscale, and is very suitable for characterizing the spin properties of thin-film materials or two-dimensional materials. MFM can distinguish different types of spin materials by analyzing magnetic domain structures. For example, ferromagnetic materials exhibit alternating bright and dark stripe patterns ($\Delta\phi > 2^\circ$), ferrimagnetic materials show blurred domain walls ($\Delta\phi \approx 0.5\text{--}2^\circ$), and topologically structured magnetic materials have bright ring-shaped stripes (with diameters ranging from 50 to 200 nm). HS materials display significant phase differences ($\Delta\phi \approx 3\text{--}5^\circ$) due to strong magnetic coupling, while LS signals are very weak ($\Delta\phi < 1^\circ$).



Moreover, the latest quantum MFM technology can achieve single-spin sensitivity at the μ_B level. Therefore, MFM plays a unique and indispensable role in analyzing spin-state variations in materials. For instance, Al-doped Co_3O_4 shows brighter MFM contrast (Fig. 3f), indicating increased surface spin states due to strain-induced electron redistribution.³⁹ Conversely, applying alternating magnetic fields to $\text{Co}_{0.8}\text{Mn}_{0.2}$ MOF reduces spin states, evidenced by MFM image darkening.⁷² MFM also resolves thickness-dependent magnetic domains: ultrathin Fe_7S_8 nanosheets (e.g., 9 nm) exhibit single-domain structures (bright contrast), while thicker ones (e.g., 48 nm) form vortex-like multi-domains (bright/dark alternation), convertible to single-domain under external fields.⁷³ For quantitative spin analysis, integrated techniques like FFT decomposition are essential, as demonstrated in CrBr_3 , where decreasing similarity indices ($\xi = 0.26$ to 0.13) with increasing thickness (190 nm to 300 nm) quantitatively confirm escalating domain complexity.⁷⁴

3.1.7 Artificial intelligence (AI) and machine learning (ML).

The rapid development of AI and ML is profoundly transforming research paradigms in the fields of electrochemical energy storage and catalysis, particularly in understanding and utilizing the key quantum property of spin. Contributions of AI/ML now extend far beyond simple assistance, playing a significant role in enhancing data analysis capabilities, accelerating research processes, and optimizing experimental design.

In the area of electrochemical catalysis, AI/ML has been instrumental in understanding and optimizing spin-related processes at reaction interfaces. First, it enables high-throughput, precise screening of spin catalysts. By constructing machine learning models with spin density, local magnetic moment, and other key descriptors, researchers can rapidly identify single or dual-atom catalysts with high activity and selectivity for target reactions from vast candidate materials. For instance, AI/ML has efficiently screened single-atom electrocatalysts for the two-electron oxygen reduction pathway.⁶⁶ Second, AI/ML can uncover the deep structure-activity relationship between spin states and catalytic performance. By quantifying the contribution of spin-related descriptors to catalytic activity, ML models translate abstract quantum effects into understandable design principles. For example, successful analysis has shown how chiral structures can enhance HER activity by inducing symmetry-breaking of spin density,⁶⁷ and how spin-spin coupling regulates reaction pathways and selectivity in CO_2 reduction processes.⁶⁸

In the realm of electrochemical energy storage, AI/ML applications focus on designing and screening electrode materials that optimize reaction kinetics and stability based on specific device requirements. The core contribution lies in the synergistic optimization and device-driven material design. Machine learning models simultaneously correlate the intrinsic properties of materials (such as conductivity, stability, and spin states of catalytic active sites) with macroscopic device performance indicators (like energy density and cycle life), enabling rapid identification of materials with multifunctional properties. For instance, high-throughput screening has been applied to identify dual-atom catalysts that exhibit both high activity (for OER/ORR) and excellent stability, directly aiding the

development of high-performance rechargeable Zn-air batteries.⁶⁹

Achieving these cutting-edge research breakthroughs heavily relies on the deep interdisciplinary integration of materials science, electrochemistry, quantum computing, and data science. A typical research paradigm is the construction of a data-driven discovery closed-loop process, with the following core steps: (1) data collection and construction: using first-principles calculations (e.g., DFT), a comprehensive dataset is generated containing material geometries, electronic structures (such as energy bands and density of states), and spin properties (e.g., magnetic moments, spin occupancy), with target properties being catalytic activity (such as overpotential and reaction free energy) or battery performance (such as capacity and stability). (2) Feature engineering: from raw quantum chemistry data, physically meaningful descriptors are extracted, selected, and constructed, including d-band centers, spin density, and charge distributions of specific atoms—these features serve as the crucial link between microscopic properties and macroscopic performance. (3) Model training and validation: appropriate machine learning algorithms (e.g., random forests, neural networks) are used to train models with the dataset, and their predictive accuracy and generalizability are rigorously evaluated through methods such as cross-validation. (4) Prediction, validation, and design: the trained, high-performing models are then used to predict the performance of a vast unknown material space, identifying the most promising candidates. These predictions are subsequently validated through first-principles calculations or experimental synthesis, completing the loop from virtual prediction to actual confirmation.

Within this complete technical workflow, feature engineering undoubtedly stands as the pivotal, decisive step. This process bridges the microscopic quantum world with macroscopic performance, and its significance is evident in the following key aspects:¹³ First, it directly determines the upper limit of machine learning model performance. Only by selecting quantum descriptors with clear physical meaning, such as d-band centers and spin occupancy, can the model capture the essential laws governing spin effects. Next, it ensures the physical interpretability of the model, transforming AI's predictions from a black box into trustworthy design principles, such as high spin density promotes hydrogen adsorption. Finally, it significantly improves data utilization efficiency, which is particularly critical for the high computational costs associated with quantum chemistry data. Therefore, feature engineering, based on profound physical insights, is the fundamental reason why AI/ML can elevate itself from a data-fitting tool to a scientific discovery engine in the field of electrochemical spin research.

For instance, ML enables systematic understanding of the intrinsic physicochemical properties of different atoms, the diversity of active sites, and the influence of interactions between sites on catalytic activity. In a study using dual-atom site catalysts with various geometric features and atomic combinations as a model system for Li-S batteries, a multi-view ML framework was constructed, comprising three components:



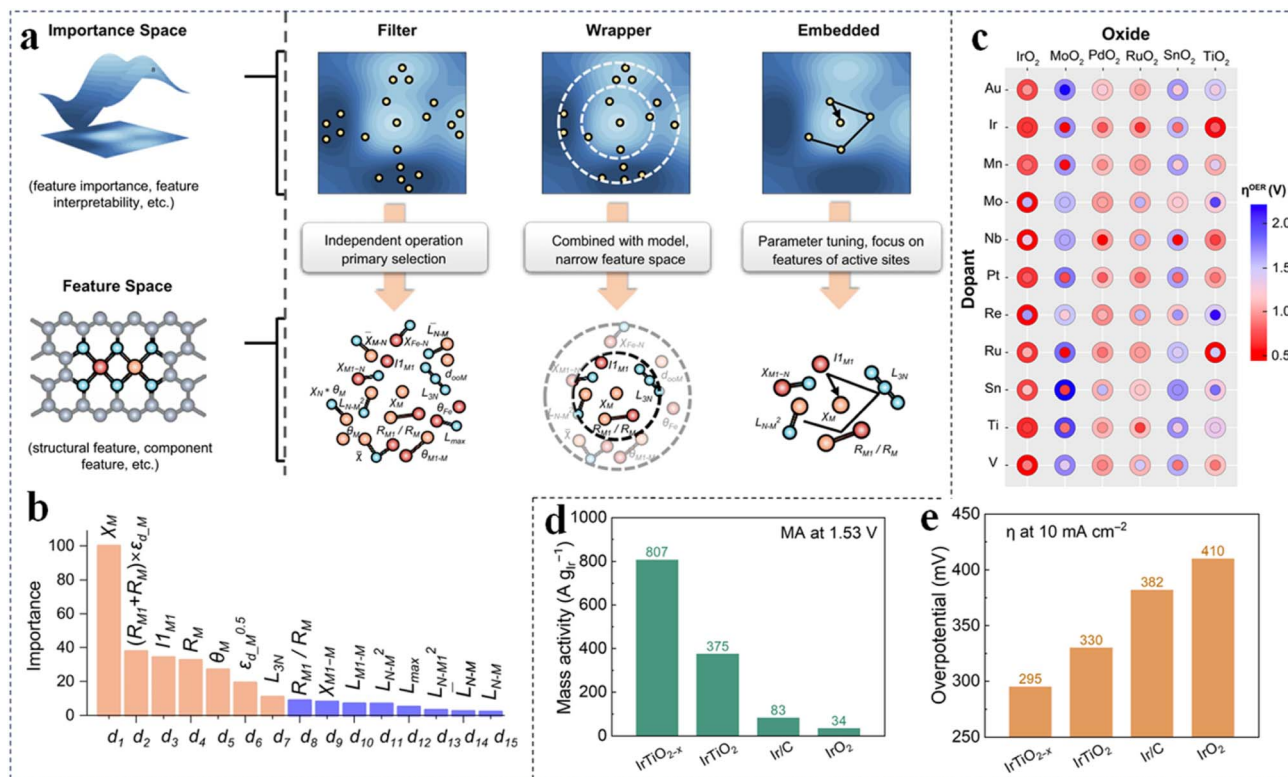


Fig. 4 (a) Schematic diagram of the multi-view machine learning framework structure. (b) Feature importance (%) of the final XGBR model based on embedded module results. Reproduced with permission.⁴⁵ Copyright 2024, Nature Publishing Group. (c) DFT-calculated heatmap of oxygen evolution reaction activity for various dopant-support combinations. (d) Overpotential of IrTiO₂, IrTiO_{2-x}, commercial IrO₂, and 20% Ir/C at 10 mA cm⁻². (e) Mass activity of IrTiO₂, IrTiO_{2-x}, commercial IrO₂, and 20% Ir/C at 1.53 V versus RHE. Reproduced with permission.⁴⁶ Copyright 2025, AAAS.

a filter module, a wrapper module, and an embedded module. Integrated analysis of limited data samples revealed that the calibrated d-orbital electronic properties exert multi-factorial influences on the performance of multi-site catalysts, thus identifying these as key features correlated with catalytic performance. This is primarily because orbital coupling between sites can induce changes in the band center and alterations in spin states, thereby affecting interactions with polysulfides, leading to various Li-S bond breaking processes and modifying lithium migration barriers (Fig. 4a and b).⁴³

In addition, integrating DFT with Bayesian optimization can accelerate the discovery of optimal doped catalyst models. This study focused on rutile-type oxide supports, where doping was achieved by substituting host atoms at coordinatively unsaturated sites with guest atoms. The calculated results of the theoretical overpotentials of each element across 66 different binary oxides revealed that Ir-doped TiO₂ exhibits potential for forming dual active sites. Further application of Gaussian process-based Bayesian optimization underscored the importance of balancing Ir content and oxygen vacancy concentration to achieve optimal performance. Subsequently, atomically dispersed Ir on TiO_{2-x} nanorods (TiO_{2-x}) was synthesized, which demonstrated an overpotential of only 295 mV at 10 mA cm⁻², outperforming commercial IrO₂ (410 mV) and 20% Ir/C (382 mV). Its mass activity reached 807 A g⁻¹ Ir, which is 9

times that of IrO₂ and 23 times that of 20% Ir/C. Although these experimental results fell short of the simulated limit, where a mass activity 40 times that of IrO₂ was predicted at an Ir surface ratio of ~12.5%, this study provided critical insights that helped narrow down the experimental design space (Fig. 4c-e).⁴⁶

With the advancement of AI technology, machine learning-assisted approaches are being applied to catalysis in increasingly profound ways. In recent years, researchers have begun integrating supervised learning, graph neural networks (GNNs), and generative models to not only predict catalytic performance but also to build interpretable structure-activity relationship models, thereby advancing catalytic theory. For example, a study employing unsupervised machine learning, using only five experimental data points combined with generalized parameter databases and problem-specific *in silico* data, successfully identified phosphine ligands capable of forming dinuclear Pd^(I) complexes from a total space of 348 ligands, with experimental verification demonstrating superior performance over conventional Pd⁽⁰⁾/Pd^(II) systems.⁷⁶

Although the aforementioned techniques each have their unique advantages in characterizing the spin states of materials or reactions, they still face certain limitations, as summarized in the table below.



Characterization techniques	Core indicators for characterizing spin	Technical advantages	Challenges for <i>in situ</i> study
XPS	Energy difference ΔE between main and satellite line	Provides direct chemical state information; highly surface-sensitive; applicable to various solid materials	Limited to surface detection; difficulty maintaining vacuum compatibility with electrochemical environments
XES	Intensity ratio of $K\beta_{1,3}/K\beta'$ peaks (HS vs. LS states)	High energy resolution; probes occupied orbital information; distinguishes coordination atoms with close atomic numbers	Weak fluorescence signals; radiation damage and absorption by window materials; complex cell design requirements
VSM	Unpaired electrons; macroscopic magnetization changes	Direct and highly sensitive measurement; determines saturation magnetization and hysteresis loops	Non-standard cell configurations may affect electrochemical performance; magnetic background interference from cell components or external fields
EPR	g value, hyperfine structure and the radical concentration	High resolution for paramagnetic centers; real-time <i>in situ</i> monitoring	Microwave absorption by metallic or electrolyte components; cell geometry constraints imposed by resonator design
Mössbauer spectroscopy	Isomer shift δ and quadrupole splitting (ΔEQ)	Provides highly precise local structural and electronic information; nondestructive analysis	Isotope enrichment required (<i>e.g.</i> , ^{57}Fe); possible deviation of reaction conditions; limited element scope
MFM	Magnetic domain structures	Non-contact measurement; high spatial resolution for magnetic domain imaging	Restricted to surface measurements; limited applicability under

(Contd.)

Characterization techniques	Core indicators for characterizing spin	Technical advantages	Challenges for <i>in situ</i> study
AI and ML	Structure–activity correlations	Enables large-scale data processing and intelligent pattern recognition	electrochemical environments Requires abundant, high-quality datasets for model reliability

3.2 *In situ* characterization techniques

While *ex situ* characterization focuses on revealing electronic spin properties of synthesized materials and their causal relationships with preparation processes, ultimately establishing structure–activity correlations through electrochemical performance. However, the advancement of *in situ* electrochemical techniques is pivotal for probing dynamic electronic structure evolution during interfacial electron transfer. This capability proves transformative for elucidating energy storage and catalytic mechanisms. Unlike *ex situ* methods, implementing *in situ* measurements requires custom-engineered electrochemical cells tailored to instrument response characteristics and material-specific spectral signatures, while rigorously mitigating signal interference from ancillary components (*e.g.*, cell materials, current collectors). The following synthesizes breakthroughs in *in situ* methodologies and their mechanistic revelations.

3.2.1 *In situ* magnetic measurements. Real-time monitoring of magnetic susceptibility enables tracking of valence changes in transition metal ions during electron transfer processes, thereby elucidating energy storage mechanisms. The measurement system (Fig. 5a) mainly consists of a Physical Property Measurement System (PPMS) integrated with a VSM module and an electrochemical testing unit.⁷⁷ The *in situ* cell must exhibit excellent electrochemical performance, compact size, and flexibility; therefore, a thin-film pouch cell encapsulated with polyethylene terephthalate (PET) is employed. To minimize the signal-to-noise ratio, the magnetic field is aligned parallel to the copper foil, and background signals (*e.g.*, magnetic moments from the copper foil, lithium metal, and PET film) are subtracted during data processing.⁷⁸ Using this method, it's possible to give interesting insight into the explanation of the excess capacity of transition metal oxides than theoretical values in battery system. Li *et al.* utilized this device to reveal anomalous electron filling in 3d orbitals during deep discharge, directly correlating with performance enhancement through an abrupt drop in magnetic susceptibility at low-voltage plateaus. Using Fe_3O_4 nanoparticles as an example, during cycling between 0.01 V and 3 V, the magnetic susceptibility followed a cyclic trend, with the first charge–discharge cycle differing due to irreversibility. Specifically, during the first





Fig. 5 (a) Scheme of *in situ* cell used for *operando* magnetometry measurements in PPMS magnetometer. Reproduced with permission.⁷⁷ Copyright 2022, American Chemical Society. (b) *In situ* magnetometry in an $\text{Fe}_3\text{O}_4/\text{Li}$ cell as a function of electrochemical cycling under an applied magnetic field of 3 T. (c) Formation of a space charge zone in the surface capacitance model for extra lithium storage. Reproduced with permission.⁷⁹ Copyright 2021, Nature Publishing Group.

cycle, the magnetism decreased from 3 V to 0.78 V, increased from 0.78 V to 0.45 V, decreased again down to 0 V, remained low until 1.4 V, and finally increased up to 3 V (Fig. 5b). These changes were correlated with structural transitions: from Fe_3O_4 spinel to $\text{FeO-Li}_2\text{O}$ composite, to Fe reduction, and finally back to Fe_3O_4 . The study confirmed that additional storage capacity originated from intermediate spin transitions and LiO_2 surface storage formation (Fig. 5c).⁷⁹ Notably, the magnetization change (16.3 emu g^{-1}) measured *via in situ* magnetometry, combined with spin polarization ratios, yielded a calculated additional capacity of 176–213 mAh g^{-1} . This closely matches the electrochemically measured value (229 mAh g^{-1}). Moreover, similar magnetic responses were observed in diverse transition metal compounds (e.g., CoO, NiO, FeF_2 , Fe_2N), demonstrating that space charge capacity is a universal mechanism in transition metal compounds.^{80–85} Crucially, particle size directly correlates with the additional capacity attained, providing novel design strategies for high-performance materials.

3.2.2 *In situ* Mössbauer spectroscopy. For *in situ* Mössbauer spectroscopy cells, electrolyte content should be minimized to avoid signal interference, and active materials should be

prepared with enriched ^{57}Fe isotopes to enhance resonance signals. Additionally, windows should use materials with weak γ -ray absorption, such as poly(methyl methacrylate) (PMMA) or Be, to prevent excessive γ -ray loss. For example, a cell suitable for LIBs (Fig. 6a), constructed with a Swagelok tube as the main body, PMMA as windows, and internal assembly in the order of lithium metal, separator, active material, and Be metal, successfully detected the conversion of FeSn_2 anode with Li_7Sn_2 and Fe during charge–discharge processes. In addition, its advanced spectral fitting capabilities further allow detailed analysis of dynamic changes in the relative proportions of different oxidation and spin states during reactions, providing breakthrough insights into the mechanisms of electrochemical energy storage and electrocatalysis.^{86–88}

For instance, Wang *et al.* revealed through *in situ* Mössbauer spectroscopy that in Prussian blue cathode materials for sodium-ion batteries, the oxidation of HS Fe^{2+} to LS Fe^{3+} dominates the initial charge capacity, while incomplete oxidation of LS Fe^{2+} during later charging stages leads to irreversible reactions between residual LS Fe^{2+} and water-coordinated HS Fe^{2+} , ultimately causing capacity loss (Fig. 6b and c).⁸⁷



Additionally, in electrocatalysis, Wang *et al.* utilized *in situ* Mössbauer spectroscopy and found that the content of *in situ* generated HS Fe⁴⁺ in NiFe-based (oxy)hydroxide (NiFe_{0.2}-O_xH_y) as an OER catalyst is positively correlated with the current density (reaction performance) (Fig. 6d), which further deepens the understanding of the mechanism of NiFe-based electrocatalysts.⁸⁹

3.2.3 *In situ* EPR. The design of the *in situ* EPR setup aims to enhance the EPR signal from the test sample while minimizing interference from background and other signals. Simultaneously, it strives to maintain the electrochemical response as close as possible to that observed in testing

environments like button cells, thereby ensuring the electrode undergoes a comprehensive energy storage or catalytic mechanism process. However, differences in EPR responses among various electrode materials necessitate specific design adaptations for the apparatus, which has thus far hindered the commercialization of standardized *in situ* fixtures. For instance, Hu *et al.* rapidly synthesized L-MnO₂ *via* laser thermal shock (83 s) and applied it as a supercapacitor electrode. *In situ* EPR, with a capillary based three electrode EPR cell (Fig. 7a and b), monitoring during charge–discharge revealed systematic changes in Mn²⁺ concentrations, with signal intensification between 0.4–0.58 V (charge) and suppression between 0.45–



Fig. 6 (a) Modified Swagelok electrochemical cell for *in situ* Mössbauer measurements. The cell (a) is composed of PFA cell body (1), nut (2), PFA sealing ferrules (3), and stainless steel plunger (4). The junction around the electrodes (b) is formed by PMMA windows (5), lithium disc (6), Be based ferrule (7), Whatman separator (8), and active material (9). Reproduced with permission.⁸⁸ Copyright 2013, American Chemical Society. (b) *Operando* ⁵⁷Fe Mössbauer spectra of monoclinic Prussian blue (M-PB) and corresponding charge/discharge profiles for two cycles. (c) Changes of LS Fe, HS Fe²⁺ and HS Fe³⁺ for two cycles. Reproduced with permission.⁸⁷ Copyright 2023, Elsevier. (d) The content of Fe⁴⁺ and corresponding electric current determined at different applied potentials. Reproduced with permission.⁸⁹ Copyright 2021, Elsevier.



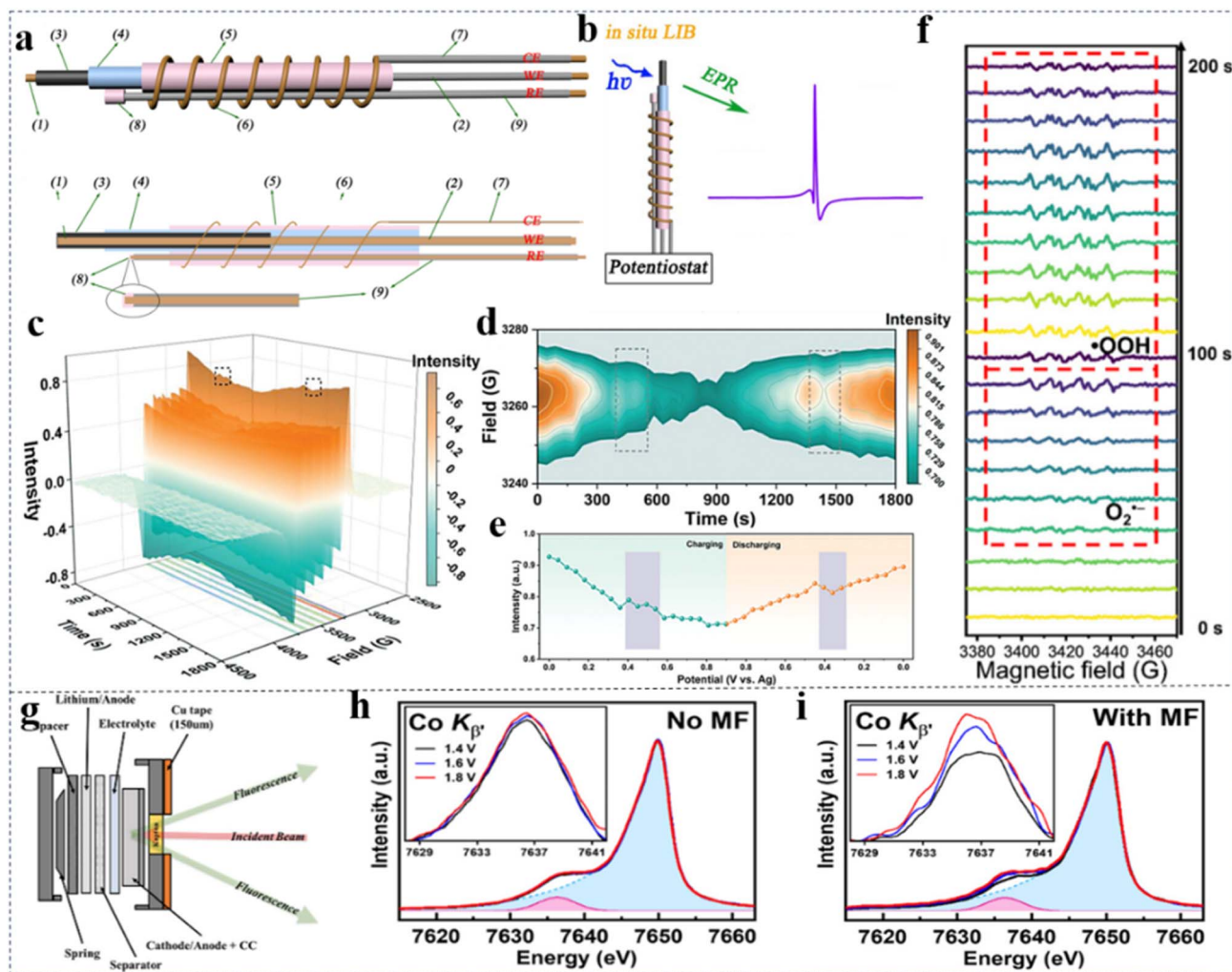


Fig. 7 (a) Scheme of the *in situ* EPR cell from Wang *et al.*: active material layer coated onto (1) the copper wire, (4) separator, (8) lithium deposited onto (9) thinner Cu wire as the ref., and (5) a thin layer of lithium film coated onto the separator and twined with Al wire as the counter electrode. (b) The working schematic diagram of *in situ* EPR cell. Reproduced with permission.⁹¹ Copyright 2021, Wiley-VCH. (c) *In situ* EPR spectra of L-MnO₂ electrode material between 2500 to 4500 G, (d) magnified EPR spectra between 3240 to 3280 G, and (e) evolution of the peak intensity. Reproduced with permission.⁹⁰ Copyright 2024, Wiley-VCH. (f) *In situ* EPR spectra of piezo-catalytic reaction. Reproduced with permission.⁹⁵ Copyright 2024, Wiley-VCH. (g) Cell design for *operando* measurements using XES. Reproduced with permission.⁹² Copyright 2024, American Chemical Society. (h) Co K β XES of CFO under different applied potentials (no magnetic field, No MF), (i) Co K β XES of CFO under different applied potentials with an external magnetic field (with MF), with the inset showing a zoom-in of the K β' features. Reproduced with permission.⁹³ Copyright 2025, American Chemical Society.

0.3 V (discharge), associated with Na⁺ intercalation and Mn valence changes (Fig. 7c–e). Compared with unmodified MnO₂, L-MnO₂ exhibited enhanced redox activity and improved Na⁺/electron transport due to optimized spin state.⁵⁵ Xu *et al.* doped Mn²⁺ into CsPbBr₃ perovskites for lithium–oxygen (Li–O₂) battery cathodes, achieving low overpotential (0.4 V) and 96.3% energy efficiency under magnetic and light stimulation. *In situ* EPR showed time-dependent spin polarization enhancement under light, confirming spin-state contributions to catalytic improvement.²⁶ In addition, in electrocatalysis, *in situ* EPR is often used to track changes in intermediates and reaction mechanisms during electrochemical reactions. Zhu *et al.* used a self-built photo/electrocatalytic *in situ* EPR test device to track the signal changes of the two-electron ORR producing H₂O₂ during electrocatalytic, photocatalytic, and piezoelectric

catalytic reactions. It was found that the ORR reaction paths of photocatalysis and piezoelectric catalysis are basically the same, *i.e.*, superoxide radicals (O₂^{•−}) first appear, then form hydroperoxyl radicals (*OOH), and finally generate H₂O₂ (O₂^{•−} → *OOH → H₂O₂) (Fig. 7f); while the reaction path in electrocatalysis only involves *OOH and *H, with no detection of O₂^{•−} (*OOH → H₂O₂). This indicates that the mechanisms of these two types of ORR reactions are different, and the piezoelectric catalytic process is closer to the photocatalytic reaction process, so its mechanism is more similar to the band theory in the field of photocatalysis.⁹⁰

3.2.4 *In situ* XES. The core design of the *in situ* XES cell (Fig. 7g) involves several key considerations: selecting a window material with low absorption for both incident X-rays and emitted fluorescence (*e.g.*, quartz, Kapton film, or Perspex);⁹²



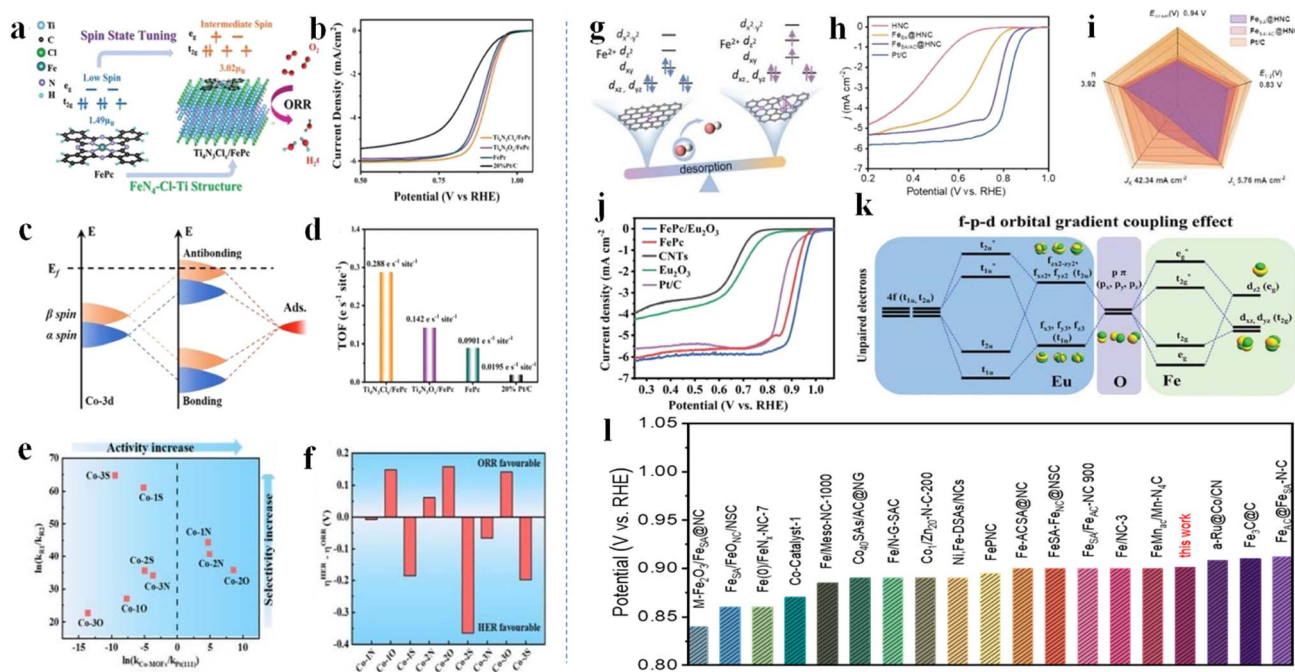


Fig. 8 (a) Schematic diagram of the spin state tuning manner. (b) Steady-state ORR polarization plots of $\text{Ti}_4\text{N}_3\text{Cl}_x/\text{FePc}$, $\text{Ti}_4\text{N}_3\text{O}_x/\text{FePc}$, FePc and 20%Pt/C performed in 0.1 M KOH at room temperature with a rotation rate of 1600 rpm, and their corresponding (c) TOF values of $\text{Ti}_4\text{N}_3\text{Cl}_x/\text{FePc}$, $\text{Ti}_4\text{N}_3\text{O}_x/\text{FePc}$, FePc , and 20% Pt/C. Reproduced with permission.⁹⁶ Copyright 2024, Wiley-VCH. (d) Schematic illustration of bond formation between the d-band center of catalyst surfaces in different spin states and the adsorbates. (e) Comparison of electrocatalytic activity and (f) product selectivity for the nine 2D Co-MOFs. Electrocatalytic selectivity between HER and ORR on the Co-MOFs. Reproduced with permission.⁹⁷ Copyright 2023 American Chemical Society. (g) Scheme of Fe atomic clusters on Fe–N–C matrix is achieved by a developed pyrolyzing method of double-ligand zinc-based zeolite framework. (h) Electrocatalytic ORR performance of the resultant catalysts and Pt/C in 0.5 M H_2SO_4 (0.1 M HClO_4 for Pt/C), and Plots of E , $E_{1/2}$, limiting current density, kinetic current density, and transfer electron number in 0.5 M H_2SO_4 . Reproduced with permission. (i) LSV curves of the catalysts. (j) Comparison of ORR activities of reported atoms and clusters in 0.1 M KOH. Reproduced with permission.⁹⁹ Copyright 2024, Wiley-VCH. (k) Illustration of the proposed f–p–d gradient orbital coupling effect in $\text{FePc}/\text{Eu}_2\text{O}_3$. Reproduced with permission.¹⁰⁰ Copyright 2025, Wiley-VCH.

excluding metal components containing elements such as Cr or Fe in the cell body to minimize stray signals, with optional matte-finishing of the inner walls to reduce specular X-ray reflection; and preferring carbon-based or organic adhesives (e.g., polytetrafluoroethylene emulsion) for sealing to avoid fluorescence interference from impurities. Furthermore, the element-specific nature of XES provides *in situ* measurements with a distinct advantage in tracking the spin-state evolution of specific elements.⁹³

For example, Chen *et al.* used *in situ* XES to detect the spin state evolution of CoFe_2O_4 (CFO) catalysts during OER with or without external magnetic field (0.4 T) intervention. They found that the spin states of Fe and Co gradually increased in the voltage range of 1.4–1.8 V, and the variation amplitude of the spin state was larger under the intervention of an external magnetic field. This explains, from the perspective of spin state, the significant impact of the external magnetic field on the CFO catalyst during the OER process, which greatly enhances the catalytic activity of this catalyst (Fig. 7h and i).⁹³ Juan Herranz *et al.* also used *in situ* XES to study the variation of the spin state of Fe–N–C catalysts with voltage during electrochemical catalysis. They found that when the voltage changed from 0.9 V to 0.2 V, the average spin state of the catalyst decreased from 0.8 to 0.55, and when the voltage recovered, the spin state also

increased and returned to its original state. This indicates that the spin state of this catalyst exhibits high reversibility with voltage changes, which provides great help for in-depth understanding of the dynamic evolution of the electronic structure of its active sites.⁹⁴ Furthermore, in electrochemical energy storage, Faisal M. Alamgir *et al.* probed the spin state changes of four different LIB cathode materials (LiCoO_2 (LCO), $\text{Li}[\text{Ni}_{1/3}\text{Co}_{1/3}\text{Mn}_{1/3}]\text{O}_2$ (NMC111), $\text{Li}[\text{Ni}_{0.8}\text{Co}_{0.1}\text{Mn}_{0.1}]\text{O}_2$ (NMC811), and LiFePO_4 (LFP)) during charging using *operando* XES. They observed distinct variations among the four materials: the intensity of the $\text{K}\beta_{1,3}$ peak gradually increased in LCO and NMC111 during charging, indicating enhanced spin states, whereas it decreased in NMC811 and LFP, suggesting diminished spin states. These findings reveal that different LIB cathode materials undergo distinct mechanisms of electronic structure changes during charge–discharge processes.⁹⁵

4 Spin electrochemical materials and their applications

4.1 Electrocatalysis

With the continuous deepening of the basic research on spin effects in electrocatalysis, studies based on spin not only analyze reaction pathways and reaction intermediates from the



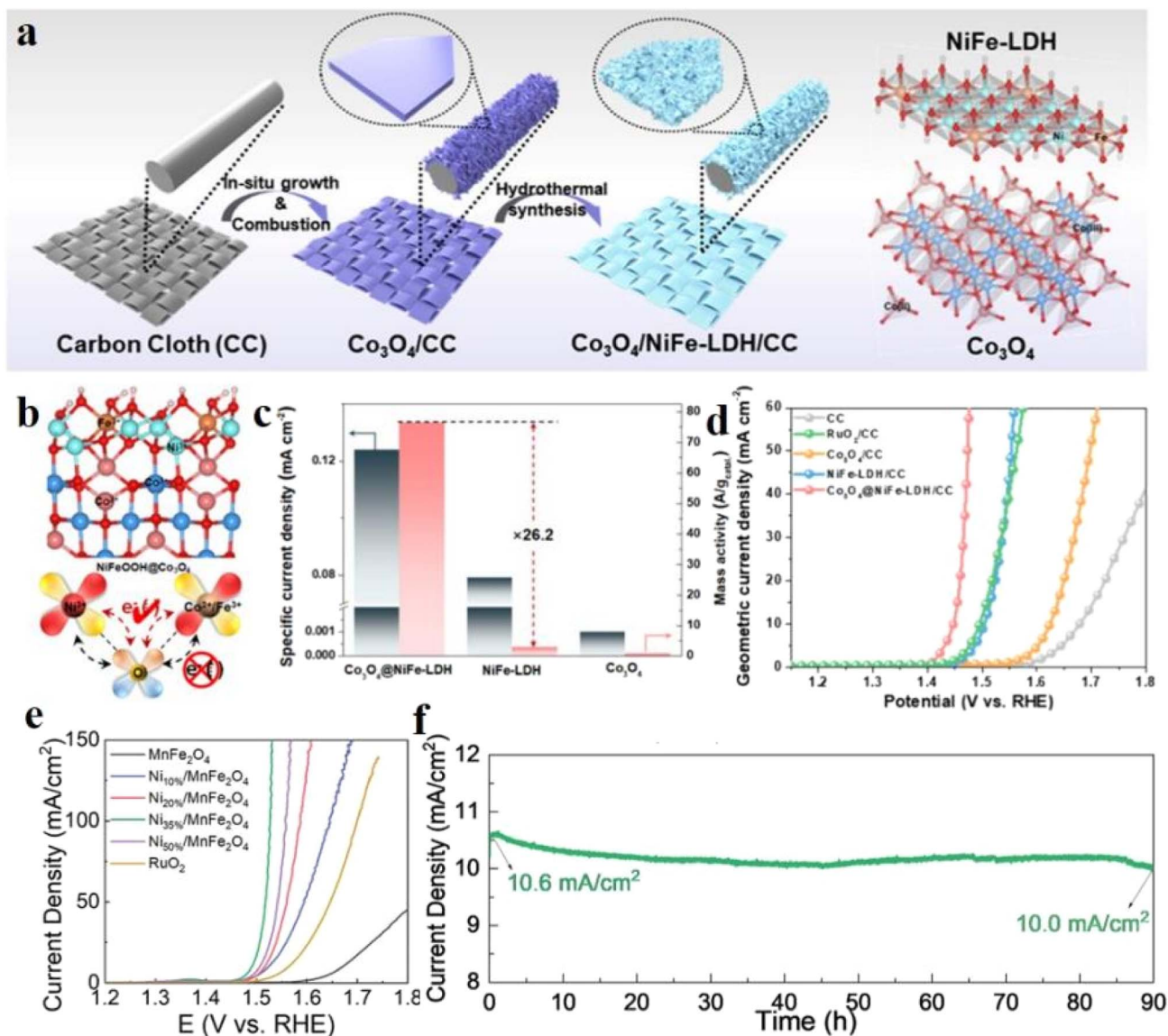


Fig. 9 (a) Schematic illustration of the synthesis process for $\text{Co}_3\text{O}_4@\text{NiFe-LDH}/\text{CC}$. (b) Slab model of $\text{NiFeOOH}@\text{Co}_3\text{O}_4$ (c) specific OER activity of $\text{Co}_3\text{O}_4@\text{NiFe-LDH}/\text{CC}$ normalized by the corresponding electrochemical surface area and catalyst mass loading at the potential of 1.48 V vs. RHE. (d) LSV curves of as-prepared samples with pure carbon cloth (CC) and RuO_2/CC as a comparison. Reproduced with permission.¹⁰¹ Copyright 2024 American Chemical Society. (e and f) LSV curves at a scan rate of 5 mV s^{-1} of MnFe_2O_4 and $\text{Ni}/\text{MnFe}_2\text{O}_4$ with different Ni loadings. Chronoamperometry test of Ni 35%/ MnFe_2O_4 at 1.50 V versus RHE. Reproduced with permission.¹⁰² Copyright 2024 Wiley-VCH.

thermodynamic perspective, but also analyze phenomena such as electron transfer from the kinetic perspective. Given the differences in reaction conditions, the mechanism of spin effects in different electrocatalytic systems needs to be systematically classified and sorted out.

4.1.1 Electrocatalytic oxygen reduction reaction (ORR). The ORR is a pivotal electrochemical process involving multi-step electron transfer and plays a central role in enabling efficient clean energy conversion technologies. Crucially, the spin state of catalysts determines the adsorption energies of key intermediates, thereby governing ORR performance. Optimization of ligand structures around central metal ions, physical field induction, and heterojunction-based gradient orbital coupling represent viable approaches for spin state manipulation.

Zhang *et al.* synthesized chlorine-terminated $\text{Ti}_4\text{N}_3\text{Cl}_x$ and oxygen-terminated $\text{Ti}_4\text{N}_3\text{O}_x$ MXenes, functionalizing them with iron phthalocyanine (FePc) to form model catalysts with well-defined $\text{FeN}_4\text{-Cl-Ti}$ and $\text{FeN}_4\text{-O-Ti}$ structures. Temperature-dependent magnetization (M-T) measurements confirmed that the $\text{FeN}_4\text{-Cl-Ti}$ structure in $\text{Ti}_4\text{N}_3\text{Cl}_x/\text{FePc}$ induces a transition from a LS state ($t_{2g}^5e_g^0$) to an intermediate-spin state ($t_{2g}^4e_g^1$), while $\text{FeN}_4\text{-O-Ti}$ in $\text{Ti}_4\text{N}_3\text{O}_x/\text{FePc}$ showed ineffective modulation (Fig. 8a).⁹⁶ This intermediate spin state enhanced ORR performance: $\text{Ti}_4\text{N}_3\text{Cl}_x/\text{FePc}$ achieved a half-wave potential ($E_{1/2}$) of +0.91 V vs. RHE, exceeding $\text{Ti}_4\text{N}_3\text{O}_x/\text{FePc}$ by 10 mV, FePc by 20 mV, and 20% Pt/C by 60 mV (Fig. 8b and c). It also exhibited a turnover frequency (TOF) of $0.288 \text{ e}^- \text{ s}^{-1} \text{ site}^{-1}$ (double than that of $\text{Ti}_4\text{N}_3\text{O}_x/\text{FePc}$ and FePc), a Tafel slope of





Fig. 10 (a) Scheme of FeW oxides. (b) LSV curves of FeWO-T and RuO₂ in 1 M KOH. Reproduced with permission.¹⁰³ Copyright 2024 Elsevier B.V. (c) Polarization curves of NiFe-LS, NiFe-HS, NiFe-KOH and V-NiFe. (d) Summarized overpotentials at current densities of 50, 100, and 500 mA cm⁻² for NiFe-LS and some representative NiFe-based catalysts. (e) Schematic illustration of the synthesis process for NiFe-LS. Reproduced with permission.¹⁰⁴ Copyright 2024 Wiley-VCH. (f) Illustration of the evolution of Fe³⁺, Co²⁺, and Ni²⁺ spin state and O-M-O spin channel; and differential charge diagram and detailed of central cations for CFL, NFL, and NCFL. (g) Polarization curves of CFL, NFL, NCFL, and CP. (h) Overpotential at 10 mA cm⁻² and 100 mA cm⁻² of CFL, NFL, and NCFL. Reproduced with permission.¹⁰⁵ Copyright 2023 American Chemical Society.

39.18 mV dec⁻¹, and a 4-electron pathway selectivity (H₂O₂ yield ≈ 4.66%). The spin-ORR linkage, established *via* DFT calculations, shows that the intermediate spin state in Ti₄N₃Cl_x/FePc facilitates electron filling in the antibonding Fe 3d and O₂ π* orbitals, optimizing O₂ activation. This reduces the energy barrier for the rate-determining step (O₂* → OOH*) and results in a lower overpotential (η = 0.47 V) compared to FePc (η = 0.85 V) and Ti₄N₃O_x/FePc (η = 0.90 V). Charge density differences confirm enhanced electron transfer to adsorbed O₂ (0.53 e⁻) in Ti₄N₃Cl_x/FePc, thus, improving ORR kinetics. In addition to the important role of functional groups in tuning spin states, the regulation of spin states through organic ligands in MOF materials can also significantly enhance their performance. Wei *et al.* conducted a systematic DFT study to investigate how organic ligand engineering modulates the spin states of Co active sites in 2D Co-MOFs and enhances their electrocatalytic performance toward the ORR.⁹⁷ By varying the ligand skeletons (benzene, triphenylene, trinaphthylene) and functional groups (-NH₂, -OH, -SH), nine Co-MOFs were designed. The triphenylene and hydroxyl (-OH)-2DCo-MOFs, Co-2O exhibited the highest magnetic moment (1.12 μ_B), indicating a HS state that correlates with enhanced ORR activity. This high spin configuration shifted the d-band center and promoted moderate adsorption of key intermediates, especially *OH, which is critical for the potential-limiting hydrogenation step. Co-2O achieved an ultralow overpotential of 0.23 V, outperforming Pt(111) and most reported catalysts (Fig. 8d). Electronic structure analysis (including PDOS and COHP) revealed that spin-state modulation altered Co-O bonding characteristics, with optimal Co 3d-O 2p orbital overlap (Fig. 8e and f).

Yu *et al.* examined multiple Fe-N₄ embedded carbon catalysts (Fe-N₄-C, Fe-N₄-C-O, Fe-N₄-C-OH, and Fe-N₄-C-OOH)

to elucidate spin effects on key ORR intermediates, which revealed that the Fe-N₄-C-OH structure exhibited an asymmetric spin distribution at the active site, where the spin density localized on the Fe atom and the adsorbed *OH intermediate was antiparallel.⁹⁸ This antiparallel spin alignment facilitated favorable orbital hybridization, leading to optimal *OH adsorption strength, which is critical for lowering the overpotential of the rate-limiting step in ORR. The PDOS indicated that this spin-state configuration altered the Fe 3d orbital occupation, shifting the d-band center and enhancing bonding interactions with *OH. As a result, the Fe-N₄-C-OH system displayed the lowest overpotential (0.38 V) among the studied models.

Spin control can also be achieved by introducing clusters around monodisperse atoms. Zhang *et al.* conducted characterizations such as hysteresis loops and ZFC-T magnetization rates to confirm that the Fe clusters reduced the 3d electron density and increased the effective magnetic moment of the single-atom Fe sites.⁹⁹ The performance enhancement was achieved by implanting Fe atomic clusters near monodispersed Fe-N₄ sites in an N-doped porous carbon matrix (Fig. 8g-i). This caused the electron spin-state of the monodispersed Fe active sites to transition from LS (t_{2g}⁶e_g⁰, μ_{eff} = 0.9 μ_B) to medium spin (MS, t_{2g}⁵e_g¹, μ_{eff} = 3.6 μ_B). DFT calculations indicated that the MS state facilitated electron filling in the σ* orbital (d_z²), weakening *OH adsorption by reducing charge transfer from Fe-N₄ to *OH and lowering the desorption energy barrier (from 0.776 to 0.532 eV). This spin-state manipulation optimized OH⁻ desorption, the rate-determining step, thereby boosting ORR activity and enabling efficient zinc-air (Zn-air) batteries.

Additionally, it is also possible to manipulate spin state by engineering heterostructures to generate qualitative gradient



spin orbital coupling. Cheng *et al.* introduced an f–p–d (Eu–O–Fe) gradient orbital coupling strategy by integrating FePc with Eu_2O_3 to enhance the spin state of atomic Fe sites. This coupling shifted the Fe center from a LS to an MS state, increasing the occupancy of electrons on the g orbitals and generating more unpaired electrons.¹⁰⁰ The elevated spin state optimized the adsorption/desorption of oxygen intermediates: bond order analysis revealed stronger binding of OOH^* (bond order: 1.5 vs. 0.5 for FePc), weakening the O–O bond to facilitate dissociation. DFT calculations confirmed reinforced OOH^* adsorption (1.37 eV vs. 1.32 eV) and significantly reduced OH^* adsorption energy (0.51 eV vs. 1.50 eV) accelerating OH^* desorption. These balanced interactions lowered the ORR energy barrier to 0.51 eV (vs. 1.17 eV for FePc) and shifted the rate-determining step from $\text{OOH}^* \rightarrow \text{O}^*$ to $\text{O}^* \rightarrow \text{OH}^*$. The f–p–d coupling also narrowed the bandgap (1.02 eV vs. 1.07 eV) and improved charge transfer, further reducing kinetic barriers (Fig. 8j and k). The ORR performance of the relevant catalysts is summarized in Fig. 8l.

4.1.2 Electrocatalytic oxygen evolution reaction (OER). For OER, its slow kinetic process is the main factor limiting the efficiency of all-oxygen reduction. Therefore, designing catalysts from the perspective of spin to improve the performance of OER is of great significance for enhancing the efficiency of overall water splitting.

Heterojunction construction represents a relatively practical and effective strategy for achieving spin-state manipulation,

thereby regulating the energy barriers of intermediate species to enhance catalytic performance. For example, the antiferromagnetic $\text{Co}_3\text{O}_4/\text{NiFe-LDH}$ coupling interface triggered spontaneous magnetic enhancement *via* strong double exchange interactions, generating polarized spin channels that accumulated spin-aligned electrons to lower the triplet O_2 formation energy barrier.¹⁰¹ This design achieved a 26-fold intrinsic OER activity boost over pristine NiFe-LDH at $\eta = 0.25$ V, with experimental/theoretical studies confirming interface induced spin electron ordering optimizes charge transfer and weakens OOH^* intermediate adsorption (Fig. 9a–d). Yang *et al.* achieved spin-state modulation in $\text{Ni/MnFe}_2\text{O}_4$ heterojunctions through interfacial charge redistribution stabilizing HS Ni^{3+} , which optimizes oxygen intermediate adsorption.¹⁰² This design delivered an ultralow 261 mV overpotential at 10 mA cm^{-2} and a 38.3 mV dec^{-1} Tafel slope, with DFT confirming reduced energy barriers *via* spin-polarized d–p coupling. The approach further enabled Zn–air batteries yielding a 1.56 V open-circuit voltage, establishing spin-engineered catalysts for ampere-level applications (Fig. 9e and f).

Crystallinity significantly influences spin properties, as demonstrated by Wang *et al.*'s FeW oxides (FeWO–T).¹⁰³ Results indicate variations in crystallinity modulate electronic interactions within Fe–W–O systems and M–O bond lengths, collectively governing spin states. The LS FeWO-450, synthesized at the critical amorphous-to-crystalline transition temperature, optimizes OER intermediate adsorption by flattening reaction



Fig. 11 (a) Mechanism of the spin-selective charge transfer of adsorbed OH^- ions through the $\text{M}(\text{O}_h)\text{--O}(1)\text{--M}(\text{O}_h)$ and the $\text{M}(\text{O}_h)\text{--O}(2)\text{--M}(\text{T}_d)$ sites in CFO. (b) LSV curves of CFO recorded in 1 M KOH electrolyte. (c) Tafel slopes of CFO recorded in 1 M KOH electrolyte. (d) Nyquist plots of CFO recorded in 1 M KOH electrolyte with and without magnetic field applied. Reproduced with permission.¹⁰⁶ Copyright 2025 American Chemical Society. (e) Schematic illustration of a three-electrode system with an external magnetic field. (f) LSV curves of the $(\text{Ru-Ni})\text{O}_x@NF$, $\text{NiO}@NF$, and NF in 1.0 M KOH. (g) Magnetization hysteresis loops of the $(\text{Ru-Ni})\text{O}_x@NF$, $\text{NiO}@NF$, NF , RuO_2 , NiO , RuO_2 (Ni-1.3%), NiO (Ru-1.1%) at room temperature. (h) Changes in η at $j = 1$ and $j = 2 \text{ A cm}^{-2}$ of the $(\text{Ru-Ni})\text{O}_x@NF$, $\text{NiO}@NF$, and NF . (i) Comparison of η at $j = 100 \text{ A cm}^{-2}$ between the $(\text{Ru-Ni})\text{O}_x@NF$ and the reported state-of-art spin selective OER catalysts. Reproduced with permission.¹⁰⁷ Copyright 2025 Wiley-VCH.



free-energy landscapes, achieving exceptional performance (289 mV@10 mA cm⁻², 41.6 mV dec⁻¹ Tafel slope). DFT results show low-crystallinity A-C-WO₃/Fe₂(WO₄)₃ exhibits the highest magnetic moment (63 μ_B), confirming its stabilized LS state that enables balanced oxygen-intermediate bonding to accelerate OER kinetics. Similarly, disrupting crystalline structures *via* doping/etching strategies introduces defects that modulate metal spin states (Fig. 10a and b). As demonstrated in Fe-modified NiFe-LDH, excessive binding between HS Fe³⁺ (t_{2g}³e_g²) and oxygen intermediates slows reaction kinetics.¹⁰⁴ Deliberately engineered defects disrupt Fe coordination environments, enhancing d-orbital splitting to stabilize LS Fe³⁺ (t_{2g}⁵e_g⁰). This optimizes adsorption of oxygen intermediates (OH*, O*, OOH*), shifting the rate-determining step from O* → OOH* on HS-Fe³⁺ to OH* → O* on LS-Fe³⁺, thus reducing energy barriers. Concurrently, accelerated formation of high-valent Ni species synergistically enhances OER kinetics (35.93 mV dec⁻¹ Tafel slope). The resulting NiFe-LS catalyst achieves a mere 244 mV overpotential at industrial-grade 500 mA cm⁻² (110 mV lower than NiFe-HS), outperforming most reported NiFe-based catalysts (Fig. 10c–e).

Complementing architectural approaches, real time spin state tuning is achievable *via* external magnetic fields without modifying catalysts. For example, Lin *et al.* demonstrated that ternary NiCoFe-LDH achieved a low overpotential (230 mV at 10 mA cm⁻²), further reduced to 206 mV under a 700 mT magnetic field, with the highest magnetic response (−34.8 mV T⁻¹).¹⁰⁵ As the spin-orbital coupling at Fe sites facilitated O–O bond formation, while the Zeeman effect optimized charge transfer.

Similar, the (Ru–Ni)_xO_x@NF catalyst achieved 200 hours stability at 286 mV (1 A cm⁻²) under a 0.4 T magnetic field. This exceptional durability originates from dual heterojunction engineering: intrinsic tuning *via* Ni-doped RuO₂ aligning Ru spins to facilitate O–O coupling, and interfacial ferromagnetic RuO₂/antiferromagnetic NiO coupling enabling spin-selective charge transfer. Theoretical analysis confirms that the resulting spin polarization minimizes intermediate spin-flip energy barriers while strengthening Ru-d/O-p hybridization (Fig. 10f–h). Huang *et al.*'s study of CoFe₂O₄ (CFO) further reveals spin order modulation under magnetic fields. Under a 0.4 T field, spin-selective electron transfer from OH⁻ reactants to Co/Fe 3d orbitals was enhanced, with Co³⁺ exhibiting greater sensitivity due to its dominant role in spin-aligned M(OH)–O(1)–M(OH) pathways that enable triplet oxygen formation (Fig. 11a–d).¹⁰⁶ This field-amplified ferrimagnetic ordering optimizes OER kinetics by promoting spin-polarized charge transfer through selective atomic channels, while M(OH)–O(2)–M(T_d) sites remain spin-inactive.

Li *et al.* boosted OER performance *via* dual spin polarization: intrinsic (Ni-doped RuO₂ aligns Ru spins, easing O–O coupling) and interfacial (FM RuO₂/AFM NiO coupling enables spin-selective charge transfer).¹⁰⁷ Under 0.4 T, (Ru–Ni)_xO_x@NF achieves 286 mV@1 A cm⁻² with 200 hours stability, supported by high coercivity and low resistance. Theoretical study shows spin polarization minimizes intermediate spin-flip energy and strengthens Ru-d/O-p hybridization, slashing reaction barriers, as shown in Fig. 11c–g.

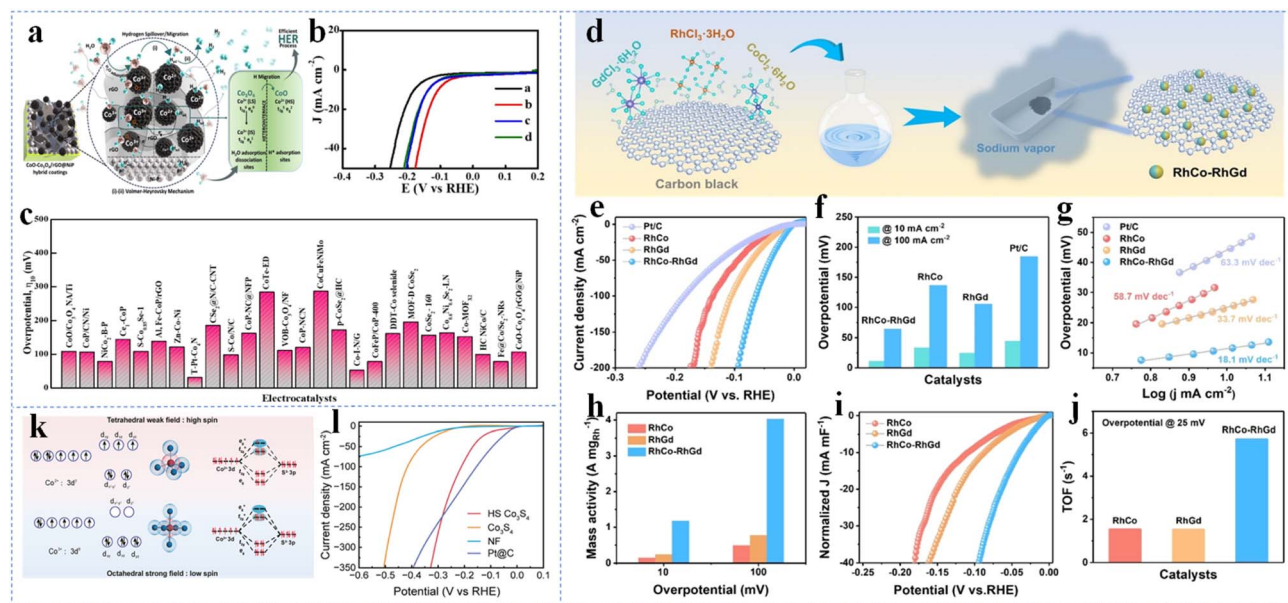


Fig. 12 (a) Schematic representation of the proposed HER mechanism of CoO–Co₃O₄/rGO@NiP. (b) LSV curves. (c) Comparison of electrochemical performance of various Co-based HER electrocatalysts with their corresponding overpotential at 10 mA cm⁻². Reproduced with permission.¹⁰⁸ Copyright 2025 American Chemical Society. (d) Schematic of the RhCo/RhGd IHA synthesis process. (e) LSV curves of RhCo, RhGd, RhCo RhGd IHAs was benchmarked against Pt/C using polarization curves. (f) Overpotentials at 10 and 100 mA cm⁻² and (g) Tafel slopes for corresponding catalysts. (h) Mass activities at overpotentials of 10 and 100 mV. (i) Normalized polarization curves against C_{dl}. (j) TOFs at overpotential of 25 mV reproduced with permission.¹¹⁰ Copyright 2024 Wiley-VCH. (k) Co Orbital Splitting (Td/OH). (l) HS-Co₃S₄ LSV performance reproduced with permission.¹¹¹ Copyright 2025 American Chemical Society.



4.1.3 Electrocatalytic hydrogen evolution reaction (HER).

The HER as the complementary half-reaction to water oxidation has been widely studied due to the high energy density of its product. Research into spin states is critical for elucidating the HER mechanism. Catalyst heterointerfaces, defects, and vacancies significantly modulate material spin density, as demonstrated by Meera *et al.*'s CoO–Co₃O₄/rGO@NiP system.¹⁰⁸ The CoO (Co²⁺ t_{2g}⁵e_g²)/Co₃O₄ (Co³⁺ t_{2g}⁶e_g⁰) heterointerface creates complementary active sites: electron-deficient Co³⁺ facilitates H₂O dissociation (Volmer step), while electron-rich Co²⁺ promotes H⁺ adsorption/H₂ release (Heyrovsky step). Oxygen vacancies elevate the Co²⁺/Co³⁺ ratio and trigger electronic rearrangement, converting LS Co³⁺ (t_{2g}⁶e_g⁰) to MS (t_{2g}⁵e_g¹). This induces J–T distortion that eliminates orbital degeneracy and accelerates charge transfer. Simultaneously, oxygen vacancies optimize adsorbate coordination environments as electron traps, while rGO enhances interphase conductivity and NiP stabilizes the architecture. Thus, the synergistic design enables efficient H-spillover, achieving 106.2 mV@10 mA cm⁻² and 107.9 mV dec⁻¹ Tafel slope (Fig. 12a–c). The spin splitting also critically influences electrocatalytic pathways. Kumar *et al.* established a direct correlation between Rashba spin splitting and HER enhancement in Janus BiClS monolayers, where broken inversion symmetry and strong spin-orbit coupling induce conduction band minimum splitting at the *T*-point, creating intermediate electronic states.¹⁰⁹ Through biaxial strain engineering, tensile strain (3%) amplified Rashba strength ($\alpha_R = 1.52$ eV Å) while reducing ΔG_H from

1.15 to 0.76 eV, whereas compressive strain diminished α_R and increased ΔG_H . DFT confirms this α_R – ΔG_H inverse relationship stems from Rashba-delayed electron–hole recombination, prolonging electron availability at conduction band minimum proximal states for HER participation.

Beyond coordination environment tuning of s–d–p orbitals, f-orbital manipulation also enables spin-state regulation. Liu *et al.* engineered RhCo–RhGd intraparticle heterostructure nanoalloys featuring distinct Gd/Co interfaces within a Rh matrix. The unique 4f electron configuration and strong orbital couplings from rare earth Gd mediates spin magnetic modulation through heterointerface induced Gd–Co antiferromagnetic interactions.¹¹⁰ These trigger electron redistribution and spin polarization control, evidenced by EPR/VSM showing reduced spin polarization and unpaired electrons. DFT further reveals weakened spin polarization at interfacial Rh/Co sites optimizes H₂O adsorption/dissociation, driving exceptional alkaline HER performance of 11.3 mV overpotential at 10 mA cm⁻² with robust stability, as shown in Fig. 12d–g. Long *et al.* engineered a HS Co₃S₄ electrocatalyst through Mo/P co-doping in spinel sulfide.¹¹¹ Mo substitution at octahedral Co sites increased tetrahedral Co²⁺ (3d⁷) populations, while P doping induced octahedral distortion. Crystal field theory confirmed unpaired electrons occupying high energy e_g^{*} orbitals in low-coordination Co sites, establishing the HS state. EPR revealed enhanced unpaired electrons at HS state ($g = 2.44$ tetrahedral signal) versus pristine Co₃S₄. DFT calculations demonstrated this HS configuration promotes d–p hybridization and e_g^{*} orbital

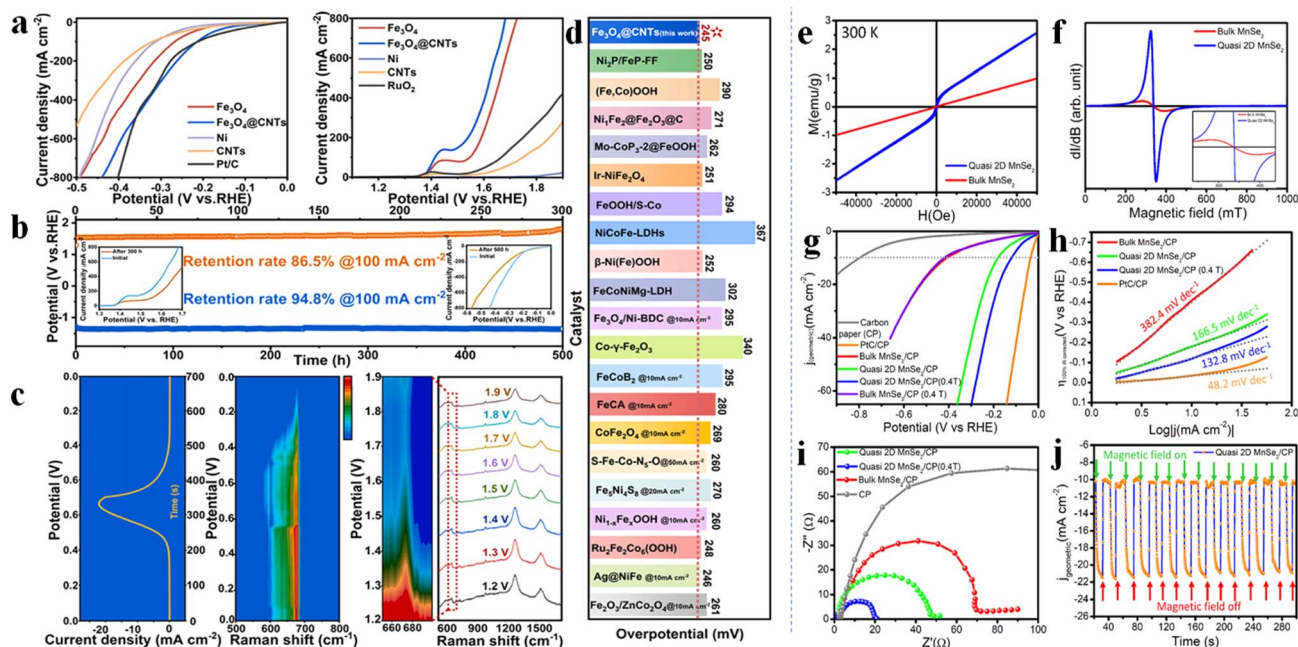


Fig. 13 (a) HER and OER LSV curves of Fe₃O₄@CNTs, Fe₃O₄, Ni foam, CNTs and commercial Pt/C in 1.0 M KOH solution. (b) Long-time chronoamperometric curves. (c) Operando Raman spectra of Fe₃O₄@CNTs. (d) OER activity of Fe₃O₄@CNTs versus recently reported Fe-based catalysts. Reproduced with permission.¹¹² Copyright 2024 Elsevier B.V. (e) M–H curve spectra for bulk and quasi-2D MnSe₂ at 300 K (f) and EPR spectra for bulk and quasi-2D MnSe₂ at 300 K. (g) LSV curves for the quasi-2D MnSe₂/CP cathode. (h) Tafel plots. (i) Nyquist plots for the quasi-2D MnSe₂/CP cathode. (j) Chronoamperometry performed with and without an external magnetic field, which was toggled at 20 seconds intervals. Reproduced with permission.¹¹³ Copyright 2024 American Chemical Society.



occupancy, accelerating electron transfer to intermediates while reducing activation energies and optimizing adsorption. Consequently, HS Co_3S_4 achieved exceptional bifunctional performance with 70 mV HER and 222 mV OER overpotentials at 10 mA cm^{-2} , as shown in Fig. 12k and l.

The external magnetic field modulation strategy also effectively applies to HER systems. Xue *et al.* demonstrated that an alternating magnetic field (AMF) induces LS to HS transitions at octahedral Fe sites in Fe_3O_4 @CNTs heterostructures.¹¹² This HS state accelerates charge transfer through enhanced $\sigma(d_z^2, p_z, s)$ and $\pi(d_{xz} - p_x, d_{yz} - p_y)$ orbital interactions, optimizing intermediate adsorption/desorption. For HER, the configuration facilitates $\sigma(d_x^2, s)$ hybridization, approaching thermoneutral ΔG of H^* intermediates. Consequently, AMF application reduced HER overpotential from 89 mV to 32 mV at 10 mA cm^{-2} (Fig. 13a–d). Complementarily, Roy *et al.* demonstrated that dimensionality tailored ferromagnetism in quasi-2D MnSe_2 ($T_c = 309 \text{ K}$, net moment: $3.54 \mu_B$ per Mn atom) enables exceptional alkaline HER enhancement under 0.4 T magnetic fields.¹¹³ Unlike paramagnetic bulk counterparts, the half-metallic ferromagnet exhibits 120% current density increase and 20.25% lower Tafel slope (132.8 vs. $166.5 \text{ mV dec}^{-1}$) at -182 mV overpotential. This originates from field-suppressed domain walls and enhanced surface spin polarization that optimize adsorbate interactions, confirmed by reproducible chronoamperometric responses during field cycling, as shown in Fig. 13e–j.

4.1.4 Electrocatalytic carbon dioxide reduction reaction (CO_2RR). The CO_2RR involves multiple processes of electron and proton transfer. Currently, there are problems such as low Faraday efficiency, poor product selectivity, and severe competition from side reactions. Similarly to HER, spin-state modulation *via* coordination environment optimization has advanced CO_2RR catalysis. Shao *et al.* systematically evaluated dual-atom spin catalysts in 2D-MOFs and zero-dimensional molecular metal complexes for selective CO_2 electroreduction.¹¹⁴ First-principles calculations across AFM, FM, and non-magnetic states revealed tunable C_1 product selectivity through spin manipulation: AFM ground state Mn_2/Fe_2 catalysts favored HCOOH production, while FM counterparts preferred CH_4 formation. This selectivity switch stems from spin dependent electronic restructuring with FM coupling elevates d-band centers to strengthen intermediate bonding (enabling deep reduction), whereas AFM configurations facilitate HCOOH desorption. Machine learning further identified absolute magnetic moment as the key activity descriptor, exhibiting linear correlation with overpotential (η). Another study focusing on tetrahedrally coordinated single-atom catalysts (SACs) revealed significant differences in electron-donating capabilities and reaction barriers among transition metal SACs anchored on ZnO basal planes.¹¹⁵ Crucially, an inverse volcano relationship emerged between SACs' spin magnetic moments and theoretical overpotentials. Among these, MS Fe^{3+} ($S = 3/2$,

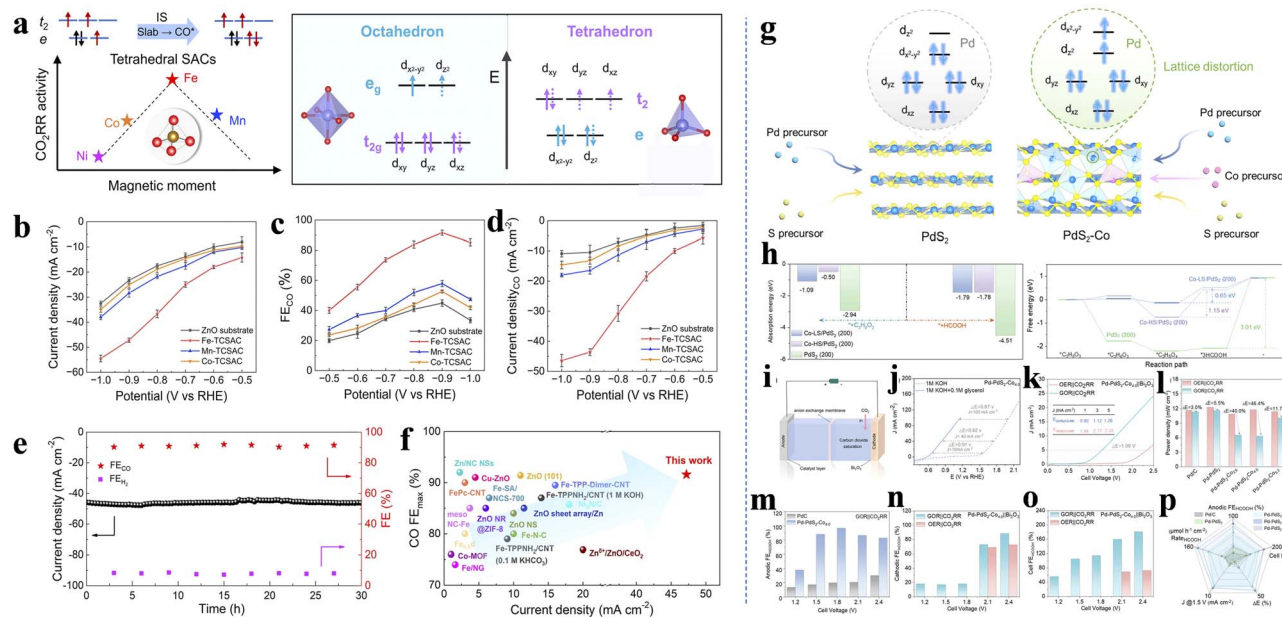


Fig. 14 (a) Electronic structures of TCSACs and schematic electron distribution. (b) Potential dependent performance of TCSACs: total current density. (c) CO. (d) Partial current density. (e) Time-dependent FE and current density of Fe-TCSAC at -0.9 V vs. RHE for CO_2RR . (f) FE_{CO} and current density of Fe-TCSACs compared with those of other recently reported Zn/Fe-based catalysts. Reproduced with permission.¹¹⁵ Copyright 2025 American Chemical Society. (g) Lattice distortion can induce different Pd d-orbital states of PdS_2 and $\text{PdS}_2\text{-Co}$ models. (h) The adsorption energy of glycerol and formic acid on three models and free energy diagram of glycerol electrooxidation to formic acid pathway on three models. (i) Scheme of integrated electrolysis cell. (j) LSV curves of $\text{Pd-PdS}_2\text{-Co}_{4.0}$. (k) The LSV curves of the integrated cell on $\text{Pd-PdS}_2\text{-Co}_{4.0}$. (l) The power density of the integrated cell at a current of 5 mA cm^{-2} . (m) The anodic FE of HCOOH in GOR coupling with CO_2RR on $\text{Pd-PdS}_2\text{-Co}_{4.0}$ and Pd/C . (n) The cathodic and (o) integrated cell FE of HCOOH on $\text{Pd-PdS}_2\text{-Co}_{4.0}$. (p) Overall performance comparison among various electrocatalysts. Reproduced with permission.¹¹⁹ Copyright 2025 Wiley-VCH.



ensuring overall electrode stability, as demonstrated by Co/C nanoparticles (Fig. 15d) delivering 880 mAh g^{-1} at 0.1 A g^{-1} with exceptional cycling durability (Fig. 15e).⁸⁴ Similarly, constructing Fe/Li₂O electrodes significantly boosts space-charge storage through enlarged electron/ion-conductor interfaces, enabling the fabricated electrode to achieve 126 mAh g^{-1} within 6 s at 50 A g^{-1} while maintaining stable performance over 30 000 cycles at 10 A g^{-1} .¹²² This spin-enhanced interfacial ion/electron transport facilitates the development of high mass loading anodes with superior rate capability. For instance, electrospun Co@CNFs (Fig. 15f) (metal Co nanoparticles into carbon nanofiber) systems allow adjustable mass loading through controlled fiber mat thickness while ensuring homogeneous nanoparticle dispersion even at high loading levels; the

resulting conductive network simultaneously promotes rapid ion diffusion in the electrolyte phase (Fig. 15g). Anodes fabricated with this method (up to 6.8 mg cm^{-2}) exhibit remarkable cycling stability and high-rate performance, sustaining over 3 mAh cm^{-2} at 2 A g^{-1} .⁸⁵ Crucially, this spatial storage mechanism circumvents phase transitions and mechanical stress, preserving electrode structural integrity for ultra-long cycling endurance.

As previously discussed, the catalytic activity of metal-nitrogen-carbon (MN_x/C) nanomaterials materials are intrinsically linked to electron spin states, which is well discussed in catalysis. When integrated into carbon anodes, the optimized electronic structure of FeN_x sites catalytically promotes reversible transformations within the SEI layer, facilitating additional

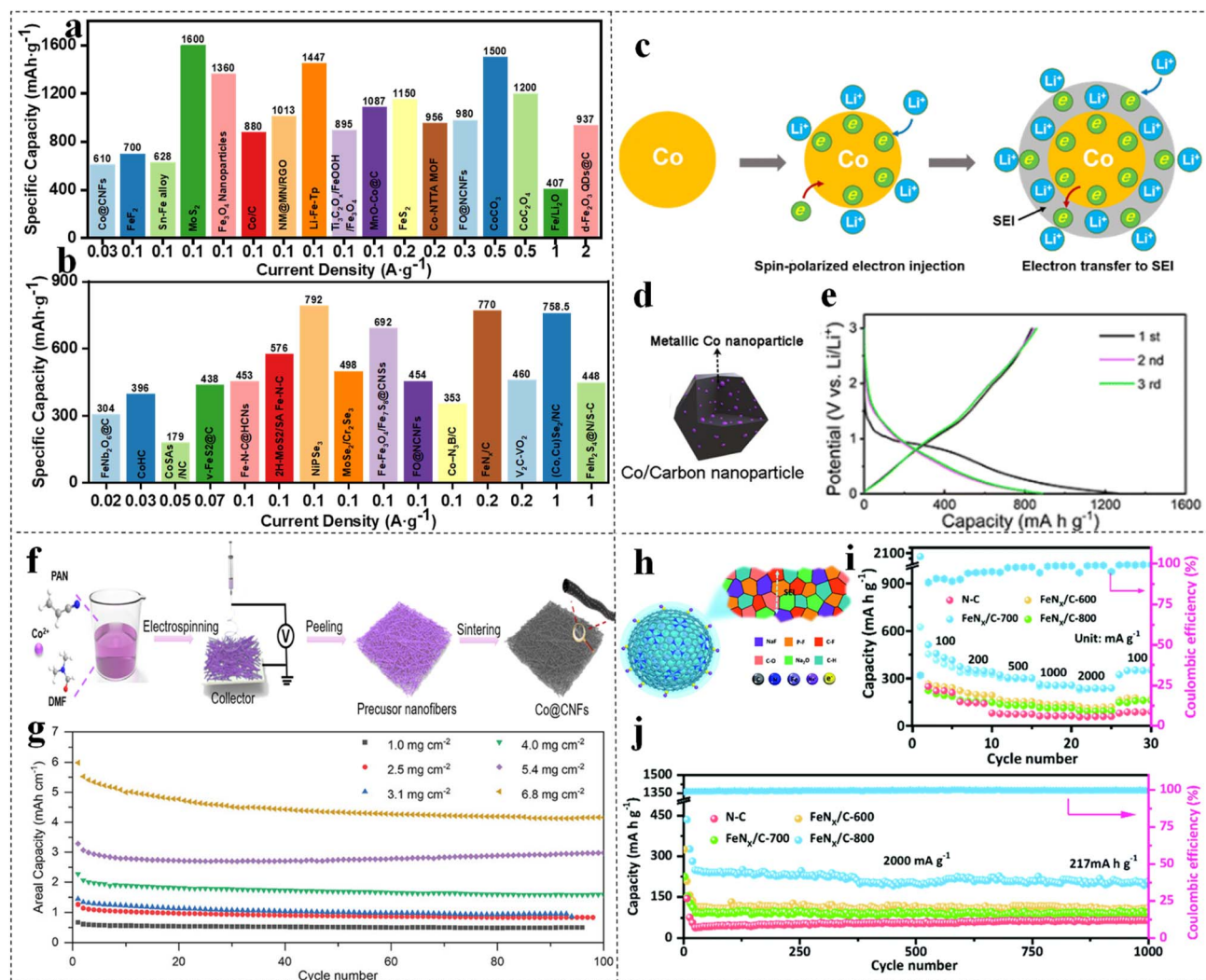


Fig. 15 Summary of the specific capacity of recent published anode materials for (a) LIBs and (b) SIBs under spin regulation. Details literature information summarized in SI. (c) Schematic illustrations of lithium storage in metallic Co via a spin-polarized electron injection to the 3d orbital of Co and subsequent electron transfer to the surrounding SEI at lower potential. (d) Schematic illustration of the Co/C NPs. (e) GCD curves of the Co/C NPs anode at a current density of 0.1 A g^{-1} between 0.01–3.0 V (vs. Li/Li⁺). Reproduced with permission.⁸⁴ Copyright 2023, the Royal Society of Chemistry. (f) Mechanism for the Co@CNFs fabrication. (g) Cycling performance of the Co@CNFs with various mass loading at a current density of 5.4 mA cm^{-2} . Reproduced with permission.¹²² Copyright 2024, Wiley-VCH. (h) Schematic illustration of SEI structures and chemistry behind Na ion storage in FeN_x/C. (i) Rate capability and (j) Long-term cyclability of NC, FeN_x/C-600, FeN_x/C-700, and FeN_x/C-800 electrodes in different electrolytes from 100 to 2000 mA g⁻¹. FeN_x/C -T denotes the FeN_x/C materials obtained at varying pyrolysis temperatures. Reproduced with permission.¹²³ Copyright 2022, the Royal Society of Chemistry.



sodium-ion storage through the cycling of both organic and inorganic SEI components (Fig. 15h).¹²³ This mechanism enables the FeN_x/C anode to deliver a high capacity of 217 mAh g^{-1} after 1000 cycles at 2000 mA g^{-1} (Fig. 15i and j). The $\text{Fe-N-C}/\text{Fe}_3\text{C}@/\text{HCNs}$ composite was synthesized *via* $\text{Fe}^{3+}/\text{PVP}$ self-assembly pyrolysis. The Fe_3C species enhance electron transfer and Na^+ adsorption, enabling a high capacity of 242 mAh g^{-1} at 2 A g^{-1} with 176 mAh g^{-1} retained after 2000 cycles.¹²⁴ Further interfacial engineering demonstrates that assembling 2H- MoS_2 nanosheets on Fe single atom (SA) anchored on N-doped carbon ($\text{Fe}(\text{SA})\text{-N-C}$) carriers induces electron transfer from $\text{Fe}(\text{SA})\text{-N-C}$ to MoS_2 (Fig. 16a) driven by work function differences.¹²⁵ This electron redistribution simultaneously enhances sodium-ion adsorption at electron-rich MoS_2 sulfur sites while modifying the spin state and catalytic activity of electron-deficient Fe sites in $\text{Fe}(\text{SA})\text{-N-C}$. Crucially, compared to N-doped carbon or pure carbon substrates, the $\text{Fe}(\text{SA})\text{-N-C}$ confined Fe sites effectively catalyze the 1T/2H- MoS_2 phase transition during cycling, thereby achieving highly efficient sodium storage. Consequently, the $\text{MoS}_2/\text{Fe}(\text{SA})\text{-N-C}$ composite maintains exceptional cyclability, retaining $\sim 350 \text{ mAh g}^{-1}$ after 2000 cycles at 2.0 A g^{-1} (Fig. 16b and c). Analogous to catalytic effects observed in metallic nanocomposites, where nanoparticle surfaces enhance spin-polarized storage, these findings suggest that coupling catalytic concepts with conventional redox/adsorption anode

mechanisms can activate inert organic-inorganic SEI components or solvent molecules, potentially unlocking substantial extra capacity.

For LIBs/SIBs featuring larger ionic radii, addressing sluggish chemical kinetics is critical to enhancing performance.¹²⁶ Spin-polarization engineering of electrode materials optimizes electronic structures to boost adsorption and phase-transition kinetics, thereby improving energy storage capabilities. In the NiPSe_3 ,¹²⁷ (theoretical capacity $>1300 \text{ mAh g}^{-1}$), the LS state of Ni^{2+} ($t_{2g}^6 e_g^2$) fully occupies the t_{2g} orbitals, generating significant electron repulsion between nickel and selenium atoms. This is reflected in the consistently low IpCOHP (Integrated projected Crystal Orbital Hamilton Population) values with minor bonding differences but fundamentally weak Ni-Se bonding energy. The weakened bond strength facilitates bond cleavage/reformation during charge/discharge cycles, effectively reducing reaction energy barriers. Enabled by this LS state structural adjustment, NiPSe_3 delivers exceptional electrochemical performance, particularly in cycling stability and rate capability: it maintains 277.3 mAh g^{-1} after 5000 cycles at 20 A g^{-1} and 249.3 mAh g^{-1} after 10 000 cycles at 15 A g^{-1} (Fig. 16d-f). Similarly, in the $(\text{Co,Cu})\text{Se}_2/\text{NC}$ electrode system,¹²⁸ electron transfer from Cu to Co fully occupies the π -symmetric t_{2g} orbitals of Co, thereby reducing spin polarization and elevating the p-band centre of Se. This enhanced electron



Fig. 16 (a) Schematic illustration of the fabrication of $\text{MoS}_2/\text{SA Fe-N-C}$. (b) Charge transfer schematic diagram of $\text{MoS}_2/\text{SA Fe-N-C}$. (c) Cycling performance of $\text{MoS}_2/\text{SA Fe-N-C}$, $\text{MoS}_2/\text{N-C}$, MoS_2/C , and MoS_2 . Reproduced with permission.¹²⁵ Copyright 2023, Wiley-VCH. (d) Schematic diagram of the crystal structure of NiPSe_3 . (e) Structural model of Ni-Se bonds in $[\text{NiSe}_6]$ octahedra in NiPSe_3 . (f) Long-term cycling performance at 15 A g^{-1} . Reproduced with permission.¹²⁷ Copyright 2025, Elsevier. (g) Schematic illustration of $\text{V}_2\text{C-VO}_2$ multi-heterostructure. (h) Simulated contour maps of K^+ ion diffusion barrier *versus* spin polarization density VH-mode. (i) Cycling stability at 0.2 A g^{-1} for V_2C and $\text{V}_2\text{C-VO}_2$ anodes. Cycling stability at 0.2 A g^{-1} for V_2C and $\text{V}_2\text{C-VO}_2$ anodes. Reproduced with permission.¹³⁰ Copyright 2022, Wiley-VCH.



repulsion between Co and Se weakens the Co–Se bond strength, while the increased sodium adsorption energy accelerates ion transfer at the electrode/electrolyte interface. Consequently, these synergistic effects significantly improve the anode's rate capability. Furthermore, constructing heterojunction interfaces induces lattice mismatch that modifies local spin polarized states. In $\text{MoSe}_2/\text{Cr}_2\text{Se}_3$ embedded within hollow carbon nanospheres, this strategy delivers a high capacity of 498 mAh g^{-1} with exceptional cycling stability (retaining 405 mAh g^{-1} after 1000 cycles at 99.8% coulombic efficiency (CE)).¹²⁹ The lattice mismatch at the $\text{MoSe}_2/\text{Cr}_2\text{Se}_3$ interface generates spin polarized states and localized magnetic moments. Through Mo^{2+} doping, the antiferromagnetic Cr_2Se_3 is effectively modified to regulate carrier concentration and spin polarization, synergistically enhancing electrochemical performance. The resulting spin polarized interfacial capacitance significantly contributes to this improvement, while selenium vacancies at the heterojunction provide abundant active sites for efficient ion intercalation/deintercalation. Similarly, in V_2C MXene/ VO_2 composites forming 3D multi-heterostructures (Fig. 16g), convergence zones with normalized charge neutrality, thus

exhibiting minimal radial spin polarization density gradients. The prepared anode demonstrates reduced pseudo-potential peaks and lower diffusion energy barriers for K^+ (Fig. 16h),¹³⁰ This enables rapid K^+ migration across the heterointerface, yielding an anode material that maintains 372 mAh g^{-1} at 0.2 A g^{-1} over 900 cycles (Fig. 16i). When assembled into flexible full cells, it withstands dynamic bending and folding deformation with negligible capacity loss even after 60 cycles.

In summary, spin-related materials significantly enhance the capacity, rate capability, and cycling stability of electrode materials in LIBs and SIBs by modulating electronic spin states. Key mechanisms include optimized spin configurations that weaken metal–ligand bonds and reduce reaction barriers, as well as heterointerface-induced spin polarization and local magnetic moments that enhance interfacial capacitance and catalytic activity. These strategies effectively alleviate mechanical stress and structural degradation, offering promising pathways for developing high-energy-density and long-life batteries. A summary of the electrochemical performance of spin-regulated anode materials is provided in Fig. 15a, b and Tables S1, S2 (SI). Furthermore, *in situ* characterization (Section

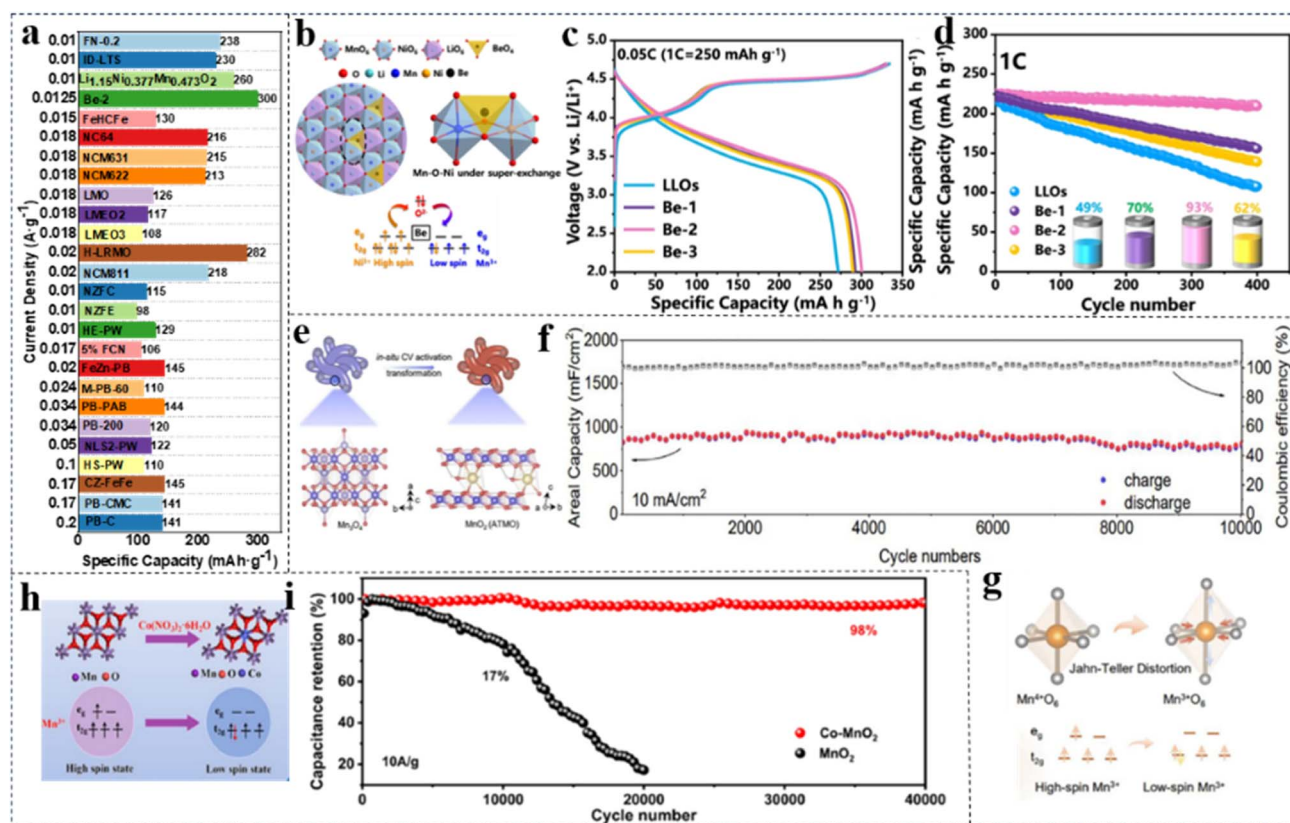


Fig. 17 (a) Summary of the specific capacity of recent published cathode materials for LIBs and SIBs under spin regulation. Details literature information summarized in SI. (b) Ni–O–Mn structure and electronic structure in Be-2. (c) Initial charge/discharge curves at 0.05C (1200 min, 12.5 mA g^{-1}). (d) Cycle performances at 1C (60 min, 250 mA g^{-1}). Herein, LLOs refers to $\text{Li}_{1.2}\text{Mn}_{0.6}\text{Ni}_{0.2}\text{O}_2$, and Be-1/2/3 correspond to $\text{Li}_{1.2}\text{Mn}_{0.6}\text{Ni}_{0.2}\text{Be}_x\text{O}_2$ ($x = 0.01, 0.02, 0.03$), respectively. Reproduced with permission.⁵⁰ Copyright, 2025 Nature Publishing Group. (e) Process for preparing activated MnO_2 (ATMO) via *in situ* electrochemical CV activation of Mn_3O_4 within different potential windows. (f) Long-term cycling performance and CE of optimal ATMO-1.0 electrode at 10 mA cm^{-2} over 10 000 cycles. (g) The J–T distortion mitigation mechanism in the $[\text{MnO}_6]$ octahedron and the spin-state transition of HS Mn^{3+} . Reproduced with permission.¹³² Copyright 2025, Wiley-VCH. (h) Co– MnO_2 synthesis strategy diagram. (i) Cycling performance for Co– MnO_2 at a current density of 10 A g^{-1} . Reproduced with permission.¹³³ Copyright 2025, Elsevier.



3.2) has revealed an interfacial space charge mechanism, suggesting the potential for catalytically activated reversible SEI transformations to provide additional storage capacity.^{80,82} This insight underscores the fundamental unity between spin-mediated electrocatalysis and energy storage. Thus, both electrocatalysis and energy storage can be regarded as different manifestations of spin-regulated electron dynamics operating under distinct energy conversion scenarios.

4.2.2 Cathodes for alkaline ion batteries. Similarly, precise manipulation of electron spin states enables multiscale coordination of electronic structure, lattice dynamics, and interfacial reactions in cathode materials, thereby overcoming structural degradation, reconstructing charge transport pathways, stabilizing redox couples, and unlocking extreme operating capabilities.

Lithium-rich cathode materials ($\text{Li}/\text{TM} > 1$) are regarded as promising candidates for enhancing LIB energy density due to their transition metal–oxygen (TMO) redox activity, high reversible capacity ($>250 \text{ mAh g}^{-1}$), and low cost. However, irreversible reactions during high-voltage anionic oxygen redox (OAR) cause severe voltage decay and energy density loss. For

instance, Be doping modulates Ni/Mn spin states to improve cathode stability: doped Be preferentially occupies tetrahedral sites in the transition metal (TM = Ni, Mn, Co, *etc*) layer, reducing Mn valence while increasing Ni valence.⁵⁰ This electron redistribution strengthens Ni–O bonds but weakens O–O bonds, forming stable Ni–(O–O) configurations that trigger strong Ni/Mn–O electronic interactions. During charging, Be doping induces intense hybridization between Ni t_{2g} and O 2p orbitals, establishing a reduction-coupling mechanism that stabilizes anionic redox. Consequently, Be-doped samples exhibit minimized structural changes and enhanced honeycomb superlattice stability, alongside increased TM migration barriers that suppress structural disorder at high voltages (Fig. 17b). These synergistic effects yield superior discharge capacity and Coulomb efficiency (CE), with Be-2 demonstrating exceptional performance, retaining 93% capacity after 400 cycles at 1C (250 mA g^{-1}), far exceeding the 49% retention of pristine materials (Fig. 17c and d). In addition, antiferromagnetic superexchange interactions can mitigate voltage decay caused by irreversible anionic oxygen redox reactions by regulating electron spin orientation during ligand-to-metal charge



Fig. 18 Summary of the specific capacity of recent published catalysts under spin regulation in (a) Li–O₂ batteries and (b) Zn–air batteries. Details literature information summarized in SI. (c) and (d) Schematic of Li–O₂ batteries with and without TBPA. (e) Cycling performances of Li–O₂ batteries with and without TBPA. Reproduced with permission.¹³⁸ Copyright 2025, American Chemical Society. (f) Schematic diagram of the crystal and spin-state structure of PtFe₂/NC (The fully-exposed PtFe₂ clusters anchored by multiwall carbon nanotubes (CNTs) with N defects). (g) Schematic illustration of the band splitting due to RKKY type interactions and the generated directional e-spins for spin-conserved electron transfer without flipping. (h) The energy conversion efficiency of PtFe₂/NC, Fe₂/NC, Pt₂/NC and commercial Pt/C electrode calculated by discharge voltage/charge voltage of the first cycle at different current density in rate performance. Reproduced with permission.¹³⁹ Copyright 2024, Wiley-VCH.



transfer. For example, introducing strongly covalent metal pairs, such as $\text{Fe}^{2+}(\text{HS})-\text{Ni}^{2+}$, $\text{Ni}^{3+}-\text{Ni}^{2+}$, $\text{Ru}^{4+}-\text{Ni}^{2+}$, or $\text{Rh}^{4+}-\text{Ni}^{2+}$, into lithium-rich layered oxide cathodes ($\text{O}_2-\text{Li}_{2/3}[\text{Li}_{1/6}\text{Mn}_{5/6}]\text{O}_2$) enables spin orientation control during charge transfer between S and Fe sites. This manipulation locks unpaired electrons from anions into ferromagnetic alignment, significantly enhancing anionic redox activity while reducing voltage hysteresis and improving reaction kinetics.¹³¹

This spin-based strategy for suppressing J-T distortion in transition metal compounds to maintain electrode structural stability demonstrates broad applicability across energy storage systems. To address MnO_2 electrode degradation,¹³² both electrochemical activation and elemental doping effectively inhibit $[\text{MnO}_6]$ octahedral distortion and Mn dissolution, thereby enabling long-term operational stability. Notably, cyclic voltammetry activation (Fig. 17e) (the activated MnO_2 phase, denoted as ATMO) (0–1.0 V vs. SCE) of Mn_3O_4 precursors generates a stabilized LS Mn^{3+} configuration ($t_{2g}^4e_g^0$) while significantly suppressing HS species, consequently mitigating J-T distortion (Fig. 17g), enhancing $[\text{MnO}_6]$ octahedral stability, and promoting reversible ion intercalation kinetics. The optimized electrode delivers an exceptional areal capacitance of $1876.6 \text{ mF cm}^{-2}$ at 1 mA cm^{-2} with robust cycling performance, retaining 91.9% capacitance after 10 000 cycles (Fig. 17f). Similarly, introducing Co into the MnO_2 (Co– MnO_2) (Fig. 17h) lattice increases t_{2g} orbital occupancy, inducing a HS to LS transition in Mn^{3+} .¹³³ This shifts electrons from the $d_{x^2-y^2}$ to d_{xy} orbital, effectively lowering the e_g orbital energy levels, thus reducing orbital degeneracy, and strengthening Mn–O bond stability. Consequently, $[\text{MnO}_6]$ octahedral distortion decreases by 69% with 80% less Mn dissolution, enabling Co– MnO_2 to maintain 98% capacity retention after 40 000 cycles at 10 A g^{-1} , dramatically superior to the pristine material's 17% retention after 20 000 cycles under identical conditions (Fig. 17i).

Spin-state engineering similarly enhances the cycling stability of Prussian Blue Analogues (PBAs) during energy storage, enabling high capacity alongside exceptional longevity as SIB cathodes. In Fe-based PBAs, carbon-coordinated iron ions adopt a LS state that forms rigid bonds with cyanide groups, increasing reaction energy barriers and rendering them electrochemically inert with minimal capacity contribution.¹³⁴ Introducing minor $\text{Cu}^{2+}/\text{Zn}^{2+}$ doping partially substitutes iron sites and strengthens Fe–N octahedral coordination in the PBA cause the activating of HS Fe redox centers with 1.6-fold enhanced activity.¹³⁵ This modification yields a remarkable initial discharge capacity of 144.7 mAh g^{-1} at 1C (170 mA g^{-1} , vs. 116 mAh g^{-1} for undoped material), while simultaneously enabling ultra-fast charging and outstanding cycling stability with 77.21% capacity retention after 2500 cycles at 10C. Low-temperature thermal activation at $200 \text{ }^\circ\text{C}$ also reactivates LS Fe in PBAs.¹³⁶ Thermodynamically driven partial cleavage of Fe–C and Fe–N bonds redistributes electron density within $[\text{FeC}_6]$ octahedra, increasing electron density around LS Fe atoms. This strongly perturbs and weakens Fe–C bonding strength, consequently reducing ligand field stabilization energy (LFSE) of $[\text{FeC}_6]$, ultimately enhancing capacity and stability. However, optimal spin states differ across PBA metal-ion systems: LS Fe

activation is desired in Fe-based PBAs, whereas Mn-based systems require LS Mn^{3+} to mitigate irreversible distortion from J-T effects in HS states.^{27,87} Therefore, spin-engineering strategies, including but not limited to doping, defect induction, and external energy-field reactivation as previously discussed, must be tailored to specific electrode material systems.¹³⁷

In summary, spin-state manipulation strategies significantly enhance the cycling stability and electrochemical performance of cathode materials in LIBs and SIBs by precisely regulating electron spin states, thereby suppressing structural degradation, stabilizing anionic redox activity, and strengthening metal–ligand bonding. This approach demonstrates broad applicability across various systems, including lithium-rich oxides, Mn-based oxides, and Prussian blue analogues. Through elemental doping, electrochemical activation, or thermal treatment, targeted induction of LS states effectively suppresses T-J distortion and enhances reversible oxygen redox, while activation of HS states improves reaction kinetics. As illustrated in Fig. 17a (Table S3, SI), recently developed high-performance spin-modulated cathode materials underscore the critical role of spin engineering in designing next-generation high-energy-density and long-life battery systems.

4.2.3 Metal oxygen battery. Catalysis and batteries have become fundamentally intertwined disciplines. While Section 4.1 comprehensively summarizes spin-state modulation strategies for enhancing electrocatalytic systems, this section focuses specifically on spin-engineered catalytic materials within battery applications.

In Li– O_2 batteries, dissolved O_2 at the cathode reacts with Li^+ during discharge to form Li_2O_2 on porous electrodes *via* the ORR, where electron transfer through the external circuit delivers electrical energy. Conversely, charging decomposes Li_2O_2 through the OER, releasing O_2 . However, commercialization faces scientific challenges including high overpotentials, low round-trip efficiency, sluggish ORR/OER kinetics, and inadequate cycle life. To address these, introducing bromine atoms into tris(4-bromophenyl)amine (TBPA) enhances SOC, enabling TBPA to form intermediate complexes with $^1\text{O}_2$.¹³⁸ This facilitates spin forbidden flip mediated oxygen state conversion ($^1\text{O}_2 \rightarrow ^3\text{O}_2$), suppressing electrolyte decomposition. When incorporated as an additive in RuO_2 -based systems, brominated TBPA elevates $^1\text{O}_2 \rightarrow ^3\text{O}_2$ conversion efficiency through SOC effects, reducing charging overpotential by 0.3 V while decreasing byproduct formation by 78%, ultimately extending cycle life to 350 cycles (Fig. 18c–e). Furthermore, constructing spin selective electron channels circumvents energy losses from non-spin conserving processes, enabling rapid electron transfer kinetics with reduced energy barriers. For instance, in a fully exposed cluster catalyst featuring Pt atoms octahedrally coordinated by six Fe atoms, ferromagnetic quantum spin exchange between Pt and Fe induces asymmetry between the spin-up and spin-down subbands on Fe (Fig. 18f and g), presenting ferromagnetic ordering of the conduction spins which arises from Ruderman–Kittel–Kasuya–Yosida (RKKY) type interactions.¹³⁹ This creates spin selective catalytic pathways where spin-conserved electron transfer between triplet O_2 and singlet



Li_2O_2 accelerates reaction kinetics, substantially lowering the energy barrier. Crucially, it renders the rate determining step from dimeric $(\text{Li}_2\text{O}_2)_2$ to Li_2O_2 during the OER, and theoretical calculations confirm significantly accelerated kinetics for the $\text{O}_2/\text{Li}_2\text{O}_2$ redox couple. Consequently, assembled Li- O_2 batteries achieve 89.6% energy conversion efficiency at 100 mA g^{-1} with ultralow discharge-charge overpotential (0.32 V) (Fig. 18h). Such catalysts, which optimize reaction kinetics through spin-selective charge transfer, can also be regulated by designing heterojunctions, as reported in the Ni/Mn Fe_2O_4 heterojunctions.¹⁴⁰

In Zn-air batteries, ORR performance critically determines overall battery efficiency, and this oxygen reduction process exhibits inherent spin dependence. Theoretical calculations reveal nitrogen species' influence on the spin state of Fe-N-C catalysts (Fig. 19a), particularly elucidating how graphitic nitrogen regulates spin configurations to enhance ORR activity.⁵¹ By strategically engineering nitrogen coordination to shift Fe active centers from LS to HS states, Wang *et al.* optimized adsorption/desorption energy barriers for oxygen intermediates, thereby boosting both catalytic activity and stability (Fig. 19b). The developed Fe-N₄/NGC-C catalyst outperforms benchmark Pt/C in ORR activity, retaining 89% of its $E_{1/2}$ after 10 000 potential cycles with merely 11 mV decay (Fig. 19c),

demonstrating exceptional durability. Assembled Zn-air batteries achieve a peak power density of 225 mW cm^{-2} and a specific capacity of $798 \text{ mAh g}_{\text{Zn}}^{-1}$ (Fig. 19d and e). Furthermore, flexible versions maintain stable discharge under bending stress and enable rapid charging of mobile devices. Similarly, one-step pyrolysis incorporates Fe_xCo_y into nitrogen-doped porous carbon to form core-shell catalysts comprising FeCo alloys encapsulated by N-doped carbon matrices ($\text{Fe}_x\text{Co}_y\text{@NPC}$) (Fig. 19f).¹⁴¹ This architecture significantly enhances catalytic activity due to work function disparities with built-in electric field at the interface from FeCo alloy to NPC layer, driving spin polarized charge transfer toward surface pyridinic-N sites. Consequently, these pyridinic-N sites develop varied magnetic moments (up to $0.024 \mu_{\text{B}}$), which are critical for OOH^* intermediate formation and substantially boost ORR activity. Zn-air batteries employing this catalyst achieve a peak power density of 282 mW cm^{-2} in liquid electrolytes (Fig. 19g), significantly surpassing that of Pt/C. Remarkably, quasi-solid-state counterparts maintain 117.6 mW cm^{-2} at $-40 \text{ }^\circ\text{C}$, representing only an 18.7% decrease from room-temperature performance, while enduring over 300 hours of continuous operation (2600 charge/discharge cycles (Fig. 19h)).

In summary, spin-engineered materials significantly enhance the performance of both Li- O_2 and Zn-air batteries by

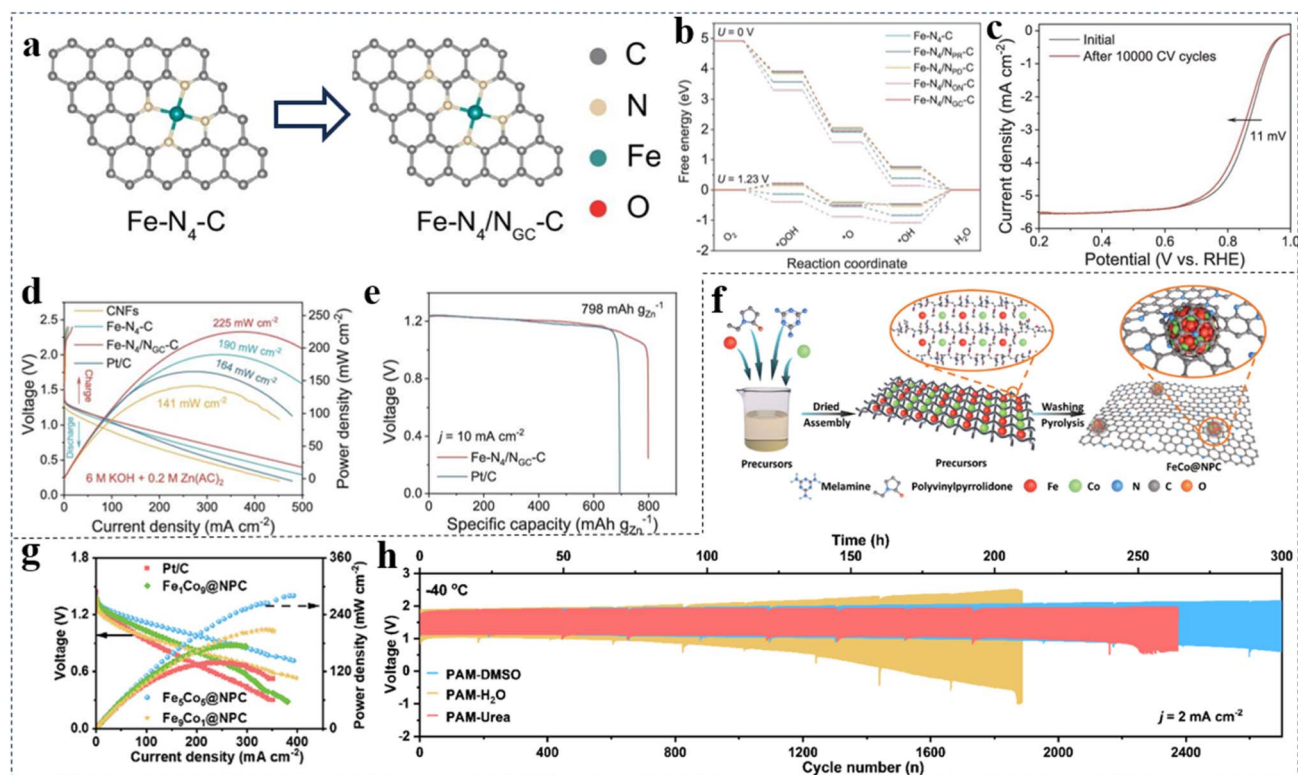


Fig. 19 (a) Structure models of Fe-N₄-C and Fe-N₄/N_{GC}-C. (b) Gibbs free energy diagrams of ORR on different structures of Fe-N-C at 0 V and 1.23 V. (c) ORR polarization LSV curves of Fe-N₄/N_{GC}-C before and after 10 000 potential cycles at a scan rate of 100 mV s^{-1} . (d) Charge and discharge polarization plots of the ZABs with Fe-N₄/N_{GC}-C as the catalyst in an aqueous electrolyte with 6 M KOH and 0.2 M Zn(CH₃COO)₂. (e) Specific capacity plots of the quasi-solid Zn-air batteries with Fe-N₄/N_{GC}-C and Pt/C as the catalysts. Reproduced with permission.⁵¹ Copyright 2025, Science China Press and Oxford University Press. (f) Schematic illustration of the synthesis of $\text{Fe}_x\text{Co}_y\text{@NPs}$. (g) Discharging polarization and power density curves of different types of $\text{Fe}_x\text{Co}_y\text{@NPs}$ and commercial Pt/C electrode. (h) Charging/discharging performance of quasi-solid Zn-air batteries at 2.0 mA cm^{-2} , $-40 \text{ }^\circ\text{C}$. Reproduced with permission.¹⁴¹ Copyright 2023, Wiley-VCH.



modulating electron spin states. In Li–O₂ batteries, spin-related strategies effectively reduce overpotentials, suppress side reactions, and extend cycle life. In Zn–air batteries, spin regulation optimizes oxygen reduction reaction kinetics, substantially improving catalytic activity and stability. The performance of recently developed advanced spin-modulated catalysts is summarized in Fig. 18a and b (Table S4 and S5, SI), demonstrating the considerable potential of this approach for metal–oxygen batteries applications.

4.2.4 Metal–sulfur battery. For metal–sulfur batteries, advancement hinges on designing efficient catalysts that simultaneously address two core bottlenecks, polysulfide shuttle and sluggish reaction kinetics, while synergistically improving sulfur utilization and electrode stability. Adjusting the spin state based on the vacancy defects of the catalyst material is one of the common strategies.¹⁴² For instance, precisely regulating oxygen vacancy concentrations in ZnAl₂O₄ modulates structural disorder and exposes Zn tetrahedral sites (Fig. 20b and c), enabling the construction of narrow-bandgap catalysts with HS states.¹⁴³ This dual optimization enhances electron transfer efficiency while reducing reaction energy barriers, thereby accelerating the multiphase conversion of lithium polysulfides (LiPSs). The amorphous ZnAl₂O₄ catalyst

maintains 93.9% capacity retention after 800 cycles even at 4C high-current density (Fig. 20d).

Coordination engineering further enhances sulfur reaction kinetics in catalysts. For example, fluorine coordination strategically modulates electronic distribution and energy level alignment at Mg(SA) sites.¹⁴⁴ Following this principle, Zhang *et al.* synthesized MgPc@FCNT (Fig. 20e and f) *via* the strategy of anchoring MgPc onto the fluorinated carbon nanotube matrix (FCNT). This configuration induces electron spin polarization that simultaneously strengthens adsorption of LiPSs intermediates and facilitates electron tunneling in Li–S batteries (Fig. 20g). As constructed electrode exhibits exceptional long-term cycling stability, demonstrating an ultralow capacity decay of 0.029% per cycle over 1000 cycles at 2C (Fig. 20h). Notably, even under high sulfur loading (4.5 mg cm⁻²), they maintain a high reversible areal capacity of 5.1 mAh cm⁻² after 100 cycles (Fig. 20i). Analogously, screening transition metals to maximize spin polarization increases spin-polarized electron density, reducing antibonding orbital occupancy in both Li₂S₂ and catalytic centers. This strengthens catalyst–sulfur interactions, weakens S–S bonds in Li₂S₂, and ultimately accelerates the Li₂S₂ → Li₂S reduction at cathode interfaces. Among ferromagnetic M–N₄ sites (M = Fe, Co, Ni),



Fig. 20 (a) Summary of the specific capacity of recent published catalysts under spin regulation in metal–sulfur batteries. Details literature information summarized in SI. (b) Spin state diagram of A-ZnAl₂O₄ and C-ZnAl₂O₄. (c) Band diagram of A-ZnAl₂O₄. (d) Long-term cycling stability of batteries. Herein, A-ZnAl₂O₄ and C-ZnAl₂O₄ refer to amorphous and crystalline ZnAl₂O₄ with high oxygen vacancy concentration, respectively. Reproduced with permission.¹⁴³ Copyright 2024, Wiley-VCH. (e) Schematic illustration of the structure of MgPc@FCNT. (f) HAADF-STEM image of MgPc@FCNT. (g) Binding energies between MgPc@FCNT, MgPc@CNT, FCNT, CNT and Li₂S_n (n = 1, 2, 4, 6, 8)/S₈. (h) Cycling performance at 2C. (i) Cycling performance under high sulfur loading at 0.1C. Reproduced with permission.¹⁴⁴ Copyright 2024, Springer Nature Link.



Fe-N₄ with the highest spin electron density delivers optimal performance.¹⁴⁵

External magnetic field induced spin polarization offers an effective strategy for boosting electrocatalytic activity, equally applicable to Li-S batteries.¹⁴⁶ Research demonstrates that CoS_x/carbon nanofiber composites (CoS_x/CNF) (Fig. 21a) prepared *via* electrospinning exhibit significantly enhanced kinetics under magnetic fields: Tafel slopes decrease to 65.3 mV dec⁻¹ for oxidation (*versus* 72.9 mV dec⁻¹ for pristine) and 45.0/27.0 mV dec⁻¹ for reduction steps (*versus* 61.2/31.0 mV dec⁻¹ for pristine) (Fig. 21b).¹⁴⁷ Concurrently, these catalysts achieve an ultralow per-cycle capacity decay of 0.0084% over 8000 cycles at 2C (Fig. 21c). Mechanistic studies reveal that external magnetic fields drive the transition of Co³⁺ from LS to HS states in CoS_x, intensifying orbital hybridization between Co-3d and S-2p orbitals. This strengthened 3d-2p hybridization accelerates interfacial charge transfer kinetics. Furthermore, electron spin polarization in CoS_x generates magnetic moments that elongate Li-S bonds, facilitating bond cleavage and thereby promoting sulfur oxidation reactions.

Spin-regulation strategies demonstrate broad applicability across Na/Al/Zn-S battery systems. For instance, when using

heteronuclear diatomic catalysts as cathodes, comprising isolated Fe-Co atomic pairs embedded in nitrogen-doped hollow carbon nanospheres (Fe-Co/NC) (Fig. 21d),¹⁴⁸ the sodium-sulfur (Na-S) batteries exhibit capacity degradation 0.018% per cycle during 2000 cycles, while delivering 341.1 mAh g⁻¹ at 5 A g⁻¹, comparing with the 810 mAh g⁻¹ under 0.5 A g⁻¹ (Fig. 21e and f). These enhancements originate from Fe-induced electron delocalization in Co(II), triggering a LS to HS transition. This electronic restructuring intensifies hybridization between Co-d_{z²} orbitals and antibonding π* orbitals of sulfur atoms in sodium polysulfides, thereby optimizing the adsorption-desorption equilibrium of sulfur intermediates on Fe-Co/NC surfaces and substantially boosting sulfur redox activity.

Similar to findings in Li-S systems, the number of unpaired electrons in a catalyst's electronic structure correlates positively with the energy position of antibonding orbitals during chalcogen hybridization. This reduces antibonding orbital occupancy, thereby enabling more efficient d-p orbital hybridization that accelerates rapid and reversible polysulfide conversion. For instance, when carbon-supported ferromagnetic SAs (Fe/Co/Ni) optimize spin polarization,¹⁴⁹ Fe-based catalysts with the highest unpaired electrons deliver superior performance as

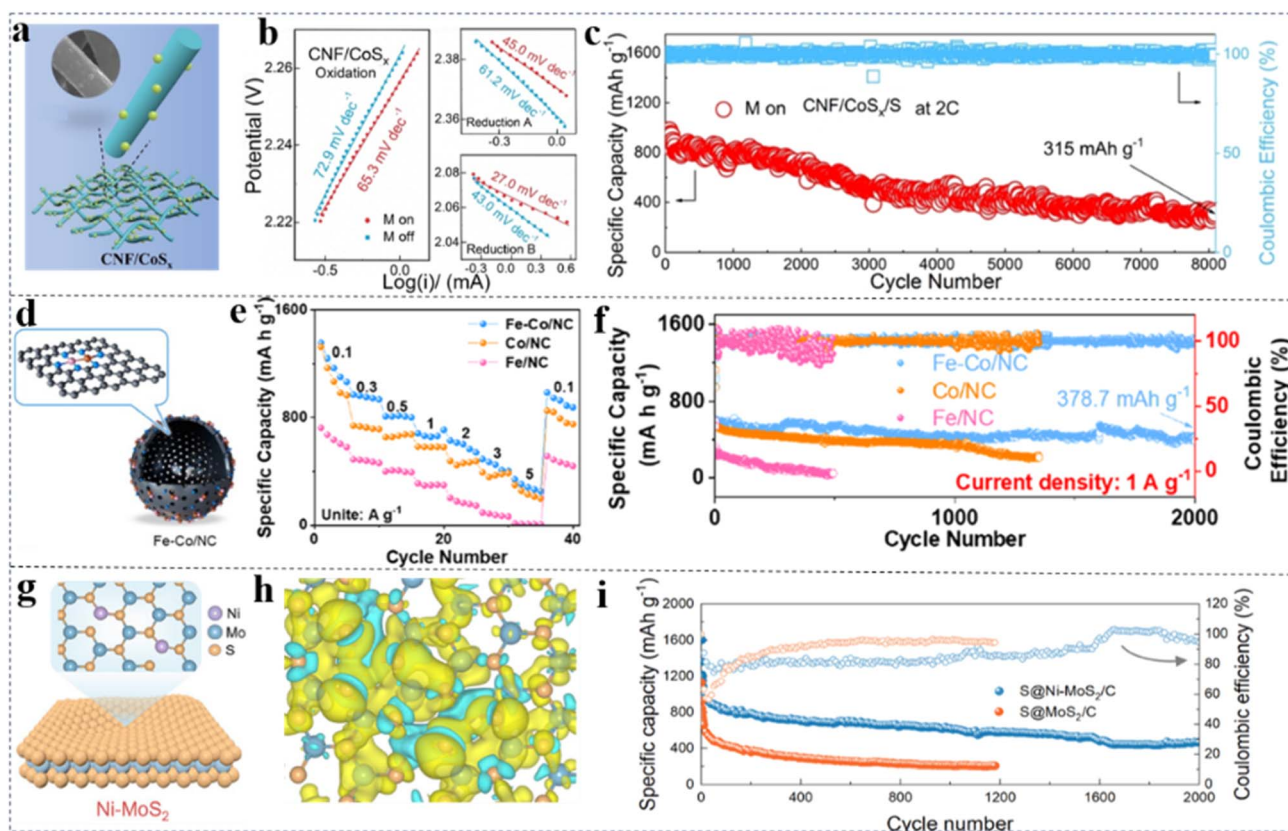


Fig. 21 (a) Schematic illustration of the structure of CNF/CoS_x. (b) The Tafel slopes of the oxidation and reduction peaks for CNF/CoS_x. Herein, reaction 1 and reaction 2 represent the two predominant reduction pathways. (c) Long-term cycling of a CNF/CoS_x/S electrode under a magnetic field. Reproduced with permission.¹⁴⁷ Copyright 2022, Wiley-VCH. (d) Schematic illustration of the structure of Fe-Co/NC. (e) Rate capabilities of a Na-S battery based on a Fe-Co/NC/S cathode containing 5.6 mg cm⁻² of S at 1 A g⁻¹. (f) Long-term cycling of a Na-S battery based on a Fe-Co/NC/S cathode containing 5.6 mg cm⁻² of S at 1 A g⁻¹. Reproduced with permission.¹⁴⁸ Copyright 2025, American Chemical Society. (g) Schematic illustration of the structure of Ni-MoS₂. (h) Calculated spin density for Ni-MoS₂ with SOC. The yellow and cyan color denote spin-up and spin-down, respectively. The iso-surfaces are 0.001 e Å⁻³. (i) Cycling performance of S@Ni-MoS₂/C and S@MoS₂/C at 0.5 A g⁻¹. Reproduced with permission.¹⁵⁰ Copyright 2025, Wiley-VCH.



cathodes in Aluminum–sulfur (Al–S) batteries. Similarly, decorating MoS₂ substrates with Ni SAs (Ni–MoS₂) (Fig. 21g) not only increases unpaired electron density but also induces spin splitting in Mo 4d orbitals, further enhancing spin polarization. This shifts sulfur from LS to HS states, optimizing aluminum polysulfide adsorption energy and consequently boosting Al–S battery performance (Fig. 21h). Ni-modified MoS₂ cathodes achieve an initial capacity of 1600 mAh g⁻¹ at 0.5 A g⁻¹ with a remarkably low per-cycle capacity decay rate of 0.035% over 2000 cycles (Fig. 21i).¹⁵⁰

In summary, spin-engineered materials play a critical role in enhancing the performance of Li–S, Na–S, and Al–S batteries by mitigating polysulfide shuttling, accelerating redox kinetics, and improving interfacial charge transfer. Key strategies include vacancy-induced spin modulation, coordination engineering, external magnetic field manipulation, and single-atom catalyst design, all of which optimize electron spin states to strengthen sulfur–catalyst interactions and facilitate efficient polysulfide conversion. The performance of recently reported advanced spin-regulated catalysts is summarized in Fig. 20a (Table S6, SI), demonstrating the broad potential of spin manipulation for advancing metal–sulfur battery technologies.

5 Conclusion and outlook

The regulation and manipulation of spin has emerged as a crucial approach in the field of electrochemical energy conversion, showing promising progress. In this review, we begin by explaining the fundamentals of electron spin theory at the atomic orbital level. We describe the characteristics of spin state transitions in electrode materials and advanced techniques for their characterization, particularly various *in situ* methods. Furthermore, we summarize the principles and effective strategies for modulating active sites. Finally, we highlight recent advances in spin-related electrochemistry for energy storage and electrocatalysis, as well as novel conversion mechanisms based on spin effects for electrochemical energy storage applications. Despite these advances, several key challenges and future research directions in this field warrant further attention, including the following aspects.

5.1 Conclusion of critical challenges

5.1.1 The structure–performance relationship concerning the spin properties of electrode materials remains unclear. For instance, there is no consensus on whether HS/MS/LS states are more favorable for optimal catalytic performance across different metal ions. A thorough and systematic characterization of the mechanisms underlying spin induced catalytic processes is essential. In particular, various *in situ* characterization techniques could track potential spin state changes of electrodes in electrolyte environments under operational conditions, and reveal evolutions in the chemical composition and electronic structure of active sites during reactions. However, the highly specific nature of these techniques and the highly customized design requirements for *in situ* instrumentation make the commercial viability of dedicated setups (*e.g.*,

for XRD or Raman) a significant challenge. This inherent lack of standardization and scalability necessitates a paradigm shift in research strategy. Consequently, fostering deep interdisciplinary collaboration and open exchange among researchers has emerged not just as an alternative, but as the most viable and effective path forward. It is also worth noting that while external magnetic fields have been shown to modulate the spin states of metal ions, it remains challenging to distinguish whether observed changes in spin characteristics arise from the strong magnetic fields inherent to techniques like EPR and PMMS, or from voltage-driven processes. On the other hand, theoretical modeling of voltage-driven dynamic evolution at electrode interfaces introduces further complexity into spin-related calculations. There is a notable scarcity of theoretical work on voltage-induced spin transfer or flipping, and detailed computational studies on spin-mediated processes in electrochemical energy conversion are still very limited.

5.1.2 Precise control over the electronic spin structure of electrode materials remains a significant challenge. Although strategies such as central atom modulation, coordination environment engineering, and metal-support interactions have been developed, based on physical mechanisms like spin-selective orbital occupation, spin ordering and polarization, and spin-orbit-charge-lattice couplings. These approaches often simultaneously alter not only the spin characteristics but also other properties such as valence state and chemical composition. As a result, the multi-faceted changes induced by these strategies make it difficult to identify the dominant factor influencing catalytic performance. Moreover, the inherent unpredictability of current spin-state control methods undermines the reliability of comparing different spin states (low, intermediate, and high spin) within the same catalyst system. There is a pressing need to establish a well-defined research framework for spin-related studies to uncover fundamental mechanisms and derive universal principles. Integrating machine learning with new methodologies capable of capturing atomic-scale evolution of lattice–spin interactions (such as potential energy surfaces) could provide deeper insights.¹⁵¹ Furthermore, leveraging the vast amount of published data, future efforts should focus on elucidating the relationships between catalytic performance and spin features, identifying meaningful descriptors, and effectively bridging computational design with experimental validation. Such advances will facilitate the rational development of tailored spin-manipulation strategies.

5.2 Outlook for future research directions

5.2.1 Promoting deep interdisciplinary integration with computer science fields such as AI/ML. The deep integration of AI with scientific disciplines is driving transformative advances across numerous fields. In the context of spin-related electrochemistry, the introduction of AI technology is expected to provide novel pathways for elucidating electrode reaction mechanisms and designing high-performance electrode materials.

Firstly, with the increasing maturity of interdisciplinary approaches, AI and ML are instigating a fundamental shift in



research paradigms. Traditional electrochemical research often relies on a combination of experimental data and theoretical models. However, the incorporation of AI enables researchers to utilize large-scale datasets and sophisticated algorithms to conduct in-depth analysis of electrode reaction mechanisms from diverse perspectives and dimensions. This transition towards a more theory-informed, data-driven approach not only accelerates research progress but also significantly enhances prediction accuracy and experimental design efficiency. Consequently, future efforts should focus on establishing systematic databases for spin-related effects, integrating the intrinsic relationships between material structure, spin state, and electrochemical performance, thereby laying a data foundation for the efficient screening of catalysts and energy storage materials. Leveraging ML and data mining techniques can extract more instructive structure–activity relationships from the growing body of computational and experimental data, steering materials research and development away from traditional empirical approaches towards precise, theory-guided design. Although this interdisciplinary field is still in a phase of rapid development, it has already demonstrated significant potential. Emerging technologies, notably large-scale language models and advanced machine learning algorithms, can deepen the analysis of material structure–activity correlations, thereby optimizing key steps such as material screening, synthesis route design, reaction mechanism simulation, scalable production, and cost assessment, ultimately leading to highly efficient utilization of time and resources. For instance, AI models like random forest and gradient boosting decision trees can rapidly predict electronic structure characteristics (e.g., d-band center and spin magnetic moment) based on theoretical calculation results and identify key descriptors influencing catalytic activity. A representative case is the work by Jun *et al.*, who combined density functional theory with AI to identify the electron spin magnetic moment as a core descriptor for oxygen reduction reaction activity in iron-based single-atom catalysts.¹⁵²

Secondly, continuous innovation at the algorithmic level is equally crucial. Future work must prioritize developing capabilities in few-shot learning, enabling the extraction of effective features from limited data to construct high-precision predictive models, thus reducing reliance on large-scale annotated experimental datasets. This highlights an urgent issue: high-quality, standardized experimental and computational data form the cornerstone of reliable AI models. Promoting data sharing and establishing collaborative platforms are key measures for ensuring the healthy development of this direction. With the refinement of theoretical models, advancements in technical tools, and deepened interdisciplinary collaboration, AI is expected to significantly accelerate the practical application of spin-related electrocatalysis in clean energy conversion and storage. The further application of large models, in particular, will advance the prediction and optimization of spin-related properties, enhance the targeting and efficiency of experiments, and gradually establish a closed-loop research system of “data-driven design—intelligent prediction—experimental verification.” Ultimately, achieving these

goals necessitates deep collaboration among materials scientists, chemists, physicists, and AI experts to collectively pioneer new scientific research paradigms.

5.2.2 Developing novel *in situ* characterization techniques with higher resolution. To deeply unravel the evolution of spin behavior in electrode materials under realistic working conditions, developing novel *in situ* characterization techniques with higher spatiotemporal resolution has become a critical direction for the field.

The primary immediate task is to overcome several limitations of existing *in situ* setups, such as discrepancies between the reaction environment and actual conditions, significant background signal interference from reaction cells, and signal attenuation caused by cell window materials. Building on this, sustained breakthroughs and innovation in cutting-edge technologies should be actively promoted. Technology routes based on synchrotron radiation sources are advancing towards miniaturization and popularization, promising to lower experimental barriers, accelerate research progress, and potentially enable real-time monitoring of spin dynamics at the atomic scale.

In the realm of precise magnetic characterization, advanced magnetic resonance techniques like low-temperature EPR, pulsed EPR, and *in situ* Nuclear Magnetic Resonance (NMR) require further enhancement of detection sensitivity. Meanwhile, emerging quantum sensing technologies, such as nitrogen-vacancy (NV) center magnetometers, are opening new research dimensions by virtue of their unique single-spin detection capabilities.

Furthermore, high priority should be given to innovative platforms and concepts based on the integration of multiple techniques. For example, combining scanning probe microscopy with various spectroscopic methods can create comprehensive characterization systems capable of simultaneously acquiring structural, electronic, and magnetic information of materials. The synergistic development of these technologies, supplemented by new machine learning-assisted data analysis methods, will progressively establish cross-scale spin analysis capability—from the atomic level to micro-devices. This will provide solid support for accurately establishing the structure–activity relationship between spin state and electrochemical performance, thereby propelling clean energy materials towards a new stage of precise design and controllable fabrication.

Author contributions

Author Xiaolin Zhang: writing – original draft for “Introduction”, “Fundamental Mechanisms of Spin-Electrochemical Coupling” and “Electrocatalysis”. Author Jinhao Pan: writing – original draft for “Advanced Characterization Techniques”, “Electrochemical energy storage” and “Conclusion and Perspective”. Author Yi Wan: literature investigation for part 2 “Fundamental Mechanisms of Spin-Electrochemical Coupling”. Author Xueqing Zheng: literature investigation for part 3.1 “*Ex Situ* Characterization Techniques”. Author Yutong Liu: literature investigation for part 3.2 “*In situ* Characterization Techniques”. Author Xingyu Liu: literature investigation for part 4.1



- 35 S. T. Zhao, W. Zhang, X. I. Zhang, C. b. Lin, W. x. Chen and G. I. Zhuang, *Adv. Theory Simul.*, 2024, 7, 2301016.
- 36 H. Tang, D. Yang, M. Lu, S. Kong, Y. Hou, D. Liu, D. Liu, S. Yan, Z. Chen and T. Yu, *J. Mater. Chem. A*, 2021, 9, 25435–25444.
- 37 Y. Du, W. Chen, Y. Wang, Y. Yu, K. Guo, G. Qu and J. Zhang, *Nano-Micro Lett.*, 2024, 16, 100.
- 38 D. Xue, Y. Zhao, J. Cao, Y. Wang, X. Li and T. Ma, *Adv. Mater.*, 2025, 2504213.
- 39 S. Y. Yao, Y. J. Ji, S. Y. Wang, Y. M. Liu, Z. S. Hou, J. R. Wang, X. Y. Gao, W. J. Fu, K. Q. Nie, J. Z. Xie, Z. Y. Yang and Y. M. Yan, *Angew. Chem., Int. Ed.*, 2024, 63, e202404834.
- 40 X. L. Wang, J. C. Wang, H. S. Hu, C. L. Yin, L. Y. Chang, Y. Zhu, J. C. Wang and M. H. Yang, *Adv. Mater.*, 2025, e202404834.
- 41 K. Sun, Y. Huang, Q. Y. Wang, W. D. Zhao, X. S. Zheng, J. Jiang and H. L. Jiang, *J. Am. Chem. Soc.*, 2024, 146, 3241–3249.
- 42 G. Greczynski and L. Hultman, *Prog. Mater. Sci.*, 2020, 107, 100591.
- 43 Z. Han, A. Chen, Z. Li, M. Zhang, Z. Wang, L. Yang, R. Gao, Y. Jia, G. Ji and Z. Lao, *Nat. Commun.*, 2024, 15, 8433.
- 44 Q. Y. Lu, *ACS Nano*, 2024, 18, 13973–13982.
- 45 J. Zhang, W. Li, R. Hoye, J. MacManus-Driscoll, M. Budde, O. Bierwagen, L. Wang, Y. Du, M. Wahila and L. Piper, *J. Mater. Chem. C*, 2018, 6, 2275–2282.
- 46 X. Niu, Y. Chen, M. Sun, S. Nagao, Y. Aoki, Z. Niu and L. Zhang, *Sci. Adv.*, 2025, 11, eadw0894.
- 47 K. Catalli, S. H. Shim, V. B. Prakapenka, J. Y. Zhao, W. Sturhahn, P. Chow, Y. M. Xiao, H. Z. Liu, H. Cynn and W. J. Evans, *Earth Planet. Sci. Lett.*, 2010, 289, 68–75.
- 48 Y. J. Ma, Y. Hu, Y. Pramudya, T. Diemant, Q. S. Wang, D. Goonetilleke, Y. S. Tang, B. Zhou, H. Hahn, W. Wenzel, M. Fichtner, Y. Ma, B. Breitung and T. Brezesinski, *Adv. Funct. Mater.*, 2022, 32, 2202372.
- 49 H. T. Li, P. Shi, L. Wang, T. R. Yan, T. Guo, X. Xia, C. Chen, J. Mao, D. Sun and L. Zhang, *Angew. Chem., Int. Ed.*, 2023, 62, e202216286.
- 50 C. L. Zheng, Y. Q. Wang, H. C. Mao, J. Zhang, X. X. Yang, J. Li, D. Zhang, X. D. Wang, F. Y. Kang and J. L. Li, *Nat. Commun.*, 2025, 16, 3900.
- 51 N. Wang, C. Meng, B. Wang, X. J. Tan, Y. Wan, Y. Yang, D. Y. Kong, W. L. Wang, F. L. Cao, A. J. Fielding, L. N. Li, M. B. Wu and H. Hu, *Natl. Sci. Rev.*, 2025, 12, nwaf061.
- 52 Y. Z. Jin, Z. Li, J. Q. Wang, R. Li, Z. Q. Li, H. Liu, J. Mao, C. K. Dong, J. Yang, S. Z. Qiao and X. W. Du, *Adv. Energy Mater.*, 2018, 8, 1703469.
- 53 L. Lin, Y. M. Xu, Y. T. Han, R. K. Xu, T. Y. Wang, Z. M. Sun and Z. H. Yan, *J. Am. Chem. Soc.*, 2024, 146, 7363–7372.
- 54 K. M. Zhao, D. X. Wu, W. K. Wu, J. B. Nie, F. S. Geng, G. Li, H. Y. Shi, S. C. Huang, H. Huang, J. Zhang, Z. Y. Zhou, Y. C. Wang and S. G. Sun, *Nat. Catal.*, 2025, 8, 422–435.
- 55 Y. Wan, T. Cao, Y. N. Li, B. Wang, W. L. Wang, Y. J. Xu, H. Yang, D. Q. Zhang, D. L. Zhang, Q. Li, C. Yu, H. Hu and M. B. Wu, *Adv. Funct. Mater.*, 2024, 34, 2311157.
- 56 A. Famulari, D. Correddu, G. Di Nardo, G. Gilardi, M. Chiesa and I. Garcia-Rubio, *J. Inorg. Biochem.*, 2022, 231, 111785.
- 57 M. A. Faraonov, E. I. Yudanova, A. V. Kuzmin, I. A. Yakushev, S. S. Khasanov, A. Otsuka, H. Yamochi, H. Kitagawa and D. V. Konarev, *Dalton Trans.*, 2023, 52, 12049–12056.
- 58 M. A. Faraonov, E. I. Yudanova, A. V. Kuzmin, I. A. Yakushev, S. S. Khasanov, A. Otsuka, H. Yamochi, H. Kitagawa and D. V. Konarev, *Dalton Trans.*, 2023, 52, 12049–12056.
- 59 D. V. Korchagin, A. V. Palii, E. A. Yureva, A. V. Akimov, E. Y. Misochko, G. V. Shilov, A. D. Talantsev, R. B. Morgunov, A. A. Shakin, S. M. Aldoshin and B. S. Tsukerblat, *Dalton Trans.*, 2017, 46, 7540–7548.
- 60 D. Y. Wu, H. Q. Yin, Z. S. Wang, M. R. Zhou, C. F. Yu, J. Wu, H. X. Miao, T. Yamamoto, W. Zhaxi, Z. T. Huang, L. Y. Liu, W. Huang, W. H. Zhong, Y. Einaga, J. Jiang and Z. M. Zhang, *Angew. Chem., Int. Ed.*, 2023, 62, e202301925.
- 61 C. Ling, M. Li, H. Li, X. Liu, F. Guo, Y. Liu, R. Zhang, J. Zhao and L. Zhang, *Nat. Commun.*, 2025, 16, 7642.
- 62 J. P. Zhao, Q. Peng, Z. J. Wang, W. Xu, H. Y. Xiao, Q. Wu, H. L. Sun, F. Ma, J. Y. Zhao, C. J. Sun, J. Z. Zhao and J. F. Li, *Nat. Commun.*, 2019, 10, 2303.
- 63 Z. Mao, J.-F. Lin, S. Huang, J. Chen, Y. Xiao and P. Chow, *Am. Mineral.*, 2013, 98, 1146–1152.
- 64 Z. N. Wang, M. T. Sougrati, Q. Zheng, R. L. Ge and J. H. Wang, *ACS Appl. Mater. Interfaces*, 2024, 16, 18908–18917.
- 65 H. J. Hou, Z. Li, Z. Y. Lu, J. Y. Shen, Z. J. Wu, J. B. Yang, K. Y. Gao and Y. F. Xia, *Int. J. Mod. Phys. B*, 2025, 39, 2550035.
- 66 X. Q. Zhang, J. M. Liu, R. Li, X. Jian, X. M. Gao, Z. L. Lu and X. P. Yue, *J. Colloid Interface Sci.*, 2023, 645, 956–963.
- 67 X. Song, Z. H. Li, L. Sheng and Y. Liu, *J. Energy Chem.*, 2025, 103, 68–78.
- 68 Y. Y. Shao and J. Zhou, *J. Colloid Interface Sci.*, 2025, 688, 548–561.
- 69 M. Tamtaji, M. G. Kim, Z. M. Li, S. H. Cai, J. Wang, P. R. Galligan, F. F. Hung, H. Guo, S. G. Chen, Z. T. Luo, W. T. Wu, W. Goddard and G. H. Chen, *Nano Energy*, 2024, 126, 109634.
- 70 D. Manikandan, I. S. Zhidkov, A. I. Kukharenko, S. O. Cholakh, E. Z. Kurmaev and R. Murugan, *Appl. Phys. A: Mater. Sci. Process.*, 2020, 126, 545.
- 71 Y. Liao, J. Liu, H. Chen, Y. Yi, X. Xi, J. Liu, L. Wang, J. Zhang, X. Z. Fu and J. L. Luo, *J. Am. Chem. Soc.*, 2025, 147, 21003–21013.
- 72 G. Zhou, P. F. Wang, H. Li, B. Hu, Y. Sun, R. Huang and L. Z. Liu, *Nat. Commun.*, 2021, 12, 4827.
- 73 T. F. Li, W. D. Zhou, C. Zhong, X. F. Luo, C. Hu, Z. Z. Jiang, H. Zhou, Y. Yang, T. Yu, W. Lei and C. L. Yuan, *ACS Energy Lett.*, 2025, 10, 958–965.
- 74 S. Y. Grebenchuk, M. Grzeszczyk, Z. L. Chen, M. Siskins, V. Borisov, M. Pereiro, M. I. Katsnelson, O. Eriksson, K. S. Novoselov and M. Koperski, *Adv. Sci.*, 2025, 12, 2500562.



- 75 S. Y. Hao, M. Y. Wang, L. S. Zhang, X. M. Lv, C. Peng, Y. H. Huang, P. Yuan, Q. Han and G. F. Zheng, *Angew. Chem., Int. Ed.*, 2025, e202510241.
- 76 J. A. Hueffel, T. Sperger, I. Funes-Ardoiz, J. S. Ward, K. Rissanen and F. Schoenebeck, *Science*, 2021, **374**, 1134–1140.
- 77 Q. Xia, X. Li, K. Wang, Z. Li, H. Liu, X. Wang, W. Ye, H. Li, X. Teng and J. Pang, *Chem. Mater.*, 2022, **34**, 5852–5859.
- 78 H. Li, Z. Hu, Q. Xia, H. Zhang, Z. Li, H. Wang, X. Li, F. Zuo, F. Zhang and X. Wang, *Adv. Mater.*, 2021, **33**, 2006629.
- 79 Q. Li, H. Li, Q. Xia, Z. Hu, Y. Zhu, S. Yan, C. Ge, Q. Zhang, X. Wang and X. Shang, *Nat. Mater.*, 2021, **20**, 76–83.
- 80 Z. Hu, F. Zhang, H. Liang, H. Zhang, H. Wang, T. Wang, R. Liu, J. Liu, Y. Li and X. Dong, *Carbon Energy*, 2022, **4**, 1011–1020.
- 81 H. Li, Z. Hu, F. Zuo, Y. Li, M. Liu, H. Liu, Y. Li, Q. Li, Y. Ding and Y. Wang, *Proc. Natl. Acad. Sci. U. S. A.*, 2024, **121**, e2320030121.
- 82 L.-Q. Zhang, Q.-T. Xia, Z.-H. Li, Y.-Y. Han, X.-X. Xu, X.-L. Zhao, X. Wang, Y.-Y. Pan, H.-S. Li and Q. Li, *Chin. Phys. Lett.*, 2022, **39**, 028202.
- 83 Z. Li, Y. Zhang, X. Li, F. Gu, L. Zhang, H. Liu, Q. Xia, Q. Li, W. Ye and C. Ge, *J. Am. Chem. Soc.*, 2021, **143**, 12800–12808.
- 84 X. Teng, X. Li, H. Yang, L. Guan, Y. Li, H. Yun, Z. Li, Q. Li, H. Hu and Z. Wang, *Chem. Sci.*, 2023, **14**, 2455–2460.
- 85 B. Wang, X. Teng, X. Li, A. J. Fielding, W. Wang, H. Liu, Z. Zhao, Y. Li, P. Iamprasertkun and L. Yang, *Adv. Funct. Mater.*, 2024, **34**, 2407494.
- 86 J. Hussain Shah, Q.-X. Xie, Z.-C. Kuang, R.-L. Ge, W.-H. Zhou, D.-R. Liu, A. I. Rykov, X.-N. Li, J.-S. Luo and J.-H. Wang, *J. Electrochem.*, 2022, **28**, 3.
- 87 Z. N. Wang, M. T. Sougrati, Y. W. He, P. N. L. Pham, W. Xu, A. Iadecola, R. L. Ge, W. H. Zhou, Q. Zheng, X. F. Li and J. H. Wang, *Nano Energy*, 2023, **109**, 108256.
- 88 M. Chamas, M. T. Sougrati, C. Reibel and P. E. Lippens, *Chem. Mater.*, 2013, **25**, 2410–2420.
- 89 Z. C. Kuang, S. Liu, X. N. Li, M. Wang, X. Y. Ren, J. Ding, R. L. Ge, W. H. Zhou, A. I. Rykov, M. T. Sougrati, P. E. Lippens, Y. Q. Huang and J. H. Wang, *J. Energy Chem.*, 2021, **57**, 212–218.
- 90 J. He, Z. Li, P. J. Feng, G. Lu, T. D. Ding, L. Chen, X. G. Duan and M. S. Zhu, *Angew. Chem., Int. Ed.*, 2024, **63**, e202410381.
- 91 B. Wang, L. W. Le Fevre, A. Brookfield, E. J. L. McInnes and R. A. W. Dryfe, *Angew. Chem., Int. Ed.*, 2021, **60**, 21860–21867.
- 92 K. Sardar, E. Petrucco, C. I. Hiley, J. D. B. Sharman, P. P. Wells, A. E. Russell, R. J. Kashtiban, J. Sloan and R. I. Walton, *Angew. Chem., Int. Ed.*, 2014, **53**, 10960–10964.
- 93 C. Y. Huang, H. A. Chen, W. X. Lin, K. H. Chen, Y. C. Lin, T. S. Wu, C. C. Chang, C. W. Pao, W. T. Chuang, J. C. Jan, Y. C. Shao, N. Hiraoka, J. W. Chiou, P. C. Kuo, J. Shiue, D. S. K. Vishnu, R. Sankar, Z. W. Cyue, W. F. Pong and C. W. Chen, *J. Am. Chem. Soc.*, 2025, **147**, 13286–13295.
- 94 V. A. Saveleva, K. Ebner, L. M. Ni, G. Smolentsev, D. Klose, A. Zitolo, E. Marelli, J. K. Li, M. Medarde, O. V. Safonova, M. Nachttegaal, F. Jaouen, U. I. Kramm, T. J. Schmidt and J. Herranz, *Angew. Chem., Int. Ed.*, 2021, **60**, 11707–11712.
- 95 A. Krishnan, D. C. Lee, I. Slagle, S. Ahsan, S. Mitra, E. Read and F. M. Alamgir, *ACS Appl. Mater. Interfaces*, 2024, **16**, 16096–16105.
- 96 S. Zhang, Y. Han, R. Zhang, Z. Zhang and G. Sun, *Adv. Energy Mater.*, 2024, **15**, 2403899.
- 97 X. Wei, C. Jiang, H. Xu, Y. Ouyang, Z. Wang, C. Lu, X. Lu, J. Pang, F. Dai and X. Bu, *ACS Catal.*, 2023, **13**, 15663–15672.
- 98 M. Yu, J. Wu, Y. Chen, Y. Du, A. Li, E. Kan and C. Zhan, *J. Mater. Chem. A*, 2024, **12**, 24530–24541.
- 99 H. Zhang, H. C. Chen, S. Feizpoor, L. Li, X. Zhang, X. Xu, Z. Zhuang, Z. Li, W. Hu, R. Snyders, D. Wang and C. Wang, *Adv. Mater.*, 2024, **36**, 2400523.
- 100 R. Cheng, X. He, M. Jiang, X. Shao, W. Tang, B. Ran, H. Li and C. Fu, *Adv. Funct. Mater.*, 2025, **35**, 2425138.
- 101 Z. Xue, B. Wu, Z. Zhang, C. Lin, X. Li, Q. Zhang and K. Tao, *ACS Catal.*, 2024, **14**, 5685–5695.
- 102 L. Yang, R. He, M. Botifoll, Y. Zhang, Y. Ding, C. Di, C. He, Y. Xu, L. Balcells, J. Arbiol, Y. Zhou and A. Cabot, *Adv. Mater.*, 2024, **36**, 2400572.
- 103 Z.-L. Wang, K.-A. Wang, X. Xiao and H.-B. Zhu, *Chem. Eng. J.*, 2024, **496**, 154218.
- 104 Y. Wang, S. Li, X. Hou, T. Cui, Z. Zhuang, Y. Zhao, H. Wang, W. Wei, M. Xu, Q. Fu, C. Chen and D. Wang, *Adv. Mater.*, 2024, **36**, 2412598.
- 105 L. Lin, R. Xin, M. Yuan, T. Wang, J. Li, Y. Xu, X. Xu, M. Li, Y. Du, J. Wang, S. Wang, F. Jiang, W. Wu, C. Lu, B. Huang, Z. Sun, J. Liu, J. He and G. Sun, *ACS Catal.*, 2023, **13**, 1431–1440.
- 106 C. Y. Huang, H. A. Chen, W. X. Lin, K. H. Chen, Y. C. Lin, T. S. Wu, C. C. Chang, C. W. Pao, W. T. Chuang, J. C. Jan, Y. C. Shao, N. Hiraoka, J. W. Chiou, P. C. Kuo, J. Shiue, D. Vishnu, S. K. R. Sankar, Z. W. Cyue, W. F. Pong and C. W. Chen, *J. Am. Chem. Soc.*, 2025, **147**, 13286–13295.
- 107 H. Li, Q. Quan, H. Dong, Y. Zhang, P. Xie, D. Chen, D. Yin, C. Y. Wong and J. C. Ho, *Adv. Funct. Mater.*, 2025, **35**, 2420810.
- 108 M. S. Meera, S. Sasidharan, S. George and S. M. A. Shibli, *ACS Appl. Energy Mater.*, 2025, **8**, 6001–6015.
- 109 D. Kumar and S. Chakraborty, *J. Mater. Chem. A*, 2024, **12**, 10287–10299.
- 110 H. Liu, Y. Jiang, Q. Li, G. Hai, C. Gu and Y. Du, *Angew. Chem., Int. Ed.*, 2024, **63**, e202412591.
- 111 Y. Long, S. Zhao, L. Wang, H. Deng, T. Sun, J. Jiang, T. Liu, S. Sun, A. Chen and H. Zhang, *ACS Catal.*, 2025, **15**, 9845–9855.
- 112 H. Xue, J. Wang, H. Cheng, H. Zhang, X. Li, J. Sun, X. Wang, L. Lin, Y. Zhang, X. Liao and Y. He, *Appl. Catal., B*, 2024, **353**, 124087.
- 113 K. Roy, R. Datta, S. Maitra and P. Kumar, *ACS Nano*, 2024, **18**, 24569–24580.
- 114 Y. Shao and J. Zhou, *J. Colloid Interface Sci.*, 2025, **688**, 548–561.
- 115 Y. Liu, X. Ren, J. Wang, H. Wang, Z. Yin, Y. Wang, W. Huang, X. Hu, Z. J. Xu and Y. Deng, *J. Am. Chem. Soc.*, 2025, **147**, 20318–20328.



- 116 Y. Li, D. Wang, Y. Guan, H. Liu, Y. Bao, N. Wu, X. Zhao, C. Sun, Z. Li, L. Lei, Y. Hou and B. Yang, *Nano Energy*, 2024, **132**, 110370.
- 117 Y. Bao, J. Xiao, Y. Huang, Y. Li, S. Yao, M. Qiu, X. Yang, L. Lei, Z. Li, Y. Hou, G. Wu and B. Yang, *Angew. Chem., Int. Ed.*, 2024, **43**, e202406030.
- 118 J. Song, D. He, X. Ma, P. Liu, W. Guo, R. Sun, F. Li, Z. Zhong, H. Zhou, J. Tang, J. Xu, T. Wu, L. Hu and Y. Wu, *J. Am. Chem. Soc.*, 2025, **147**, 16198–16206.
- 119 P. Liu, H. Ma, Y. Qin, J. Li, F. Li, J. Ye, Q. Guo, N. Su, C. Gao, L. Xie, X. Sheng, S. Zhao, G. Jiang, Y. Ren, Y. Sun and Z. Zhang, *Angew. Chem., Int. Ed.*, 2025, e202506032.
- 120 P. Balaya, H. Li, L. Kienle and J. Maier, *Adv. Funct. Mater.*, 2003, **13**, 621–625.
- 121 B. Wang, X. L. Teng, X. K. Li, A. J. Fielding, W. L. Wang, H. J. Liu, Z. Q. Zhao, Y. Q. Li, P. Iamprasertkun, L. J. Yang, N. T. Ruiz, Q. Li, M. B. Wu and H. Hu, *Adv. Funct. Mater.*, 2024, **34**, 2407494.
- 122 L. Y. Zhao, T. S. Wang, F. K. Zuo, Z. Y. Ju, Y. H. Li, Q. Li, Y. Zhu, H. S. Li and G. H. Yu, *Nat. Commun.*, 2024, **15**, 3778.
- 123 H. C. Xia, L. X. Zan, G. Qu, Y. C. Tu, H. L. Dong, Y. F. Wei, K. X. Zhu, Y. Yu, Y. F. Hu, D. H. Deng and J. A. Zhang, *Energy Environ. Sci.*, 2022, **15**, 771–779.
- 124 H. C. Xia, P. F. Yuan, L. X. Zan, G. Qu, Y. C. Tu, K. X. Zhu, Y. F. Wei, Z. Y. Wei, F. Y. Zheng, M. Zhang, Y. F. Hu, D. H. Deng and J. N. Zhang, *Nano Res.*, 2021, **8**, 7154–7162.
- 125 H. C. Xia, L. X. Zan, P. F. Yuan, G. Qu, H. L. Dong, Y. F. Wei, Y. Yu, Z. Y. Wei, W. F. Yan, J. S. Hu, D. H. Deng and J. N. Zhang, *Angew. Chem., Int. Ed.*, 2023, **62**, e202218282.
- 126 S. L. Zang, C. Hu, L. J. Nie, H. Chen, X. Q. Yu, M. T. Ma and J. Zheng, *Sustainable Mater. Technol.*, 2022, **33**, e00480.
- 127 C. Li, T. Liu, Z. Wang, X. Cao, C. Zhu and D. Li, *J. Colloid Interface Sci.*, 2025, 138494.
- 128 D. D. Wang, Y. F. Chao, K. Y. Guo, Z. S. Wang, M. X. Yang, J. H. Zhu, X. W. Cui and Q. Xu, *Adv. Funct. Mater.*, 2024, **34**, 2405642.
- 129 X. C. Wang, X. Zhang, Y. Chen, J. Q. Dong and J. Zhao, *Small*, 2024, **20**, 2312130.
- 130 M. Y. Xu, D. Zhou, T. L. Wu, J. Qi, Q. Du and Z. B. Xiao, *Adv. Funct. Mater.*, 2022, **32**, 2203263.
- 131 Z. W. Jiang, K. Zhang, Q. H. Ding, C. Gao, Y. X. Zuo, H. C. Wang, J. F. Cai, B. Li, X. P. Ai and D. G. Xia, *J. Am. Chem. Soc.*, 2025, **147**, 3062–3071.
- 132 X. S. Cui, Q. F. Wu, S. Y. Wang, J. Z. Wang, W. L. Qubie, Y. X. Zhang, J. L. Zhang and J. C. Fu, *Small*, 2025, e05422.
- 133 Z. Y. Zhang, J. Zheng, X. Y. Chen, X. Y. Yu, L. J. Li, L. X. Bao, J. Peng and X. Li, *Energy Storage Mater.*, 2025, **76**, 104128.
- 134 X. Gao, L. L. Guo, S. J. Zhang, H. Q. Li, N. Chen, Y. H. Han, B. H. He, P. Y. Ma, W. S. Gao and Y. X. Bai, *Angew. Chem., Int. Ed.*, 2025, e202421916.
- 135 D. Yang, H. N. Wang, Y. Zhao, M. T. Guo, D. Xie, N. K. Wang, F. Wang, C. P. Wang, T. Y. Li, Y. He, M. Y. Ruan and Q. Li, *Adv. Funct. Mater.*, 2025, 2503067.
- 136 W. W. Fu, G. Wang, K. Zhang, J. F. Zheng, C. Y. Zhang, J. Y. Wang, J. W. Li, J. Zheng, M. Zhang and Z. R. Shen, *J. Power Sources*, 2025, **641**, 236866.
- 137 X. H. Bai, Z. H. Zhang, J. Tao, T. Li, X. Y. Chen, R. Sun, Y. Ren, H. B. He, S. M. Qiu, D. Huang, J. Xu and X. C. Yin, *Adv. Funct. Mater.*, 2025, 2509513.
- 138 Z. L. Jiang, B. Wen, Y. H. Huang, Y. Z. Wang, H. Y. Fang and F. J. Li, *J. Am. Chem. Soc.*, 2025, **147**, 10992–10998.
- 139 Y. Rao, J. W. Yang, J. M. Tian, W. J. Ning, S. H. Guo and H. S. Zhou, *Angew. Chem., Int. Ed.*, 2025, **64**, e202418893.
- 140 L. L. Yang, R. He, M. Botifoll, Y. C. Zhang, Y. Ding, C. Di, C. S. He, Y. Xu, L. Balcells, J. Arbiol, Y. T. Zhou and A. Cabot, *Adv. Mater.*, 2024, **36**, 2400572.
- 141 Y. F. Wei, H. C. Xia, H. H. Lan, D. P. Xue, B. Zhao, Y. Yu, Y. F. Hu and J. N. Zhang, *Adv. Energy Mater.*, 2024, **14**, 2303011.
- 142 Z. Huang, X. C. Jiao, J. Lei, Y. Z. Zuo, Z. Wang, L. L. Lu, J. Dong, W. Yan and J. J. Zhang, *Nano Energy*, 2025, **139**, 110979.
- 143 F. Zhou, Z. Q. Gong, R. H. Wang, M. R. Guo, R. Zeng, Y. Li, Z. Xiao, L. Qie and J. W. Liu, *Adv. Funct. Mater.*, 2025, **35**, 2417730.
- 144 Y. Du, W. J. Chen, Y. Wang, Y. Yu, K. Guo, G. Qu and J. N. Zhang, *Nano-Micro Lett.*, 2024, **16**, 100.
- 145 R. Yan, Z. Y. Zhao, M. H. Cheng, Z. Yang, C. Cheng, X. K. Liu, B. Yin and S. Li, *Angew. Chem., Int. Ed.*, 2023, **62**, e202215414.
- 146 J. Yu, C. Huang, O. Usoltsev, A. P. Black, K. Gupta, M. C. Spadaro, I. Pinto-Huguet, M. Botifoll, C. H. Li, J. Herrero-Martín, J. Y. Zhou, A. Ponrouch, R. R. Zhao, L. Balcells, C. Y. Zhang, A. Cabot and J. Arbiol, *ACS Nano*, 2024, **18**, 19268–19282.
- 147 C. Y. Zhang, C. Q. Zhang, G. W. Sun, J. L. Pan, L. Gong, G. Z. Sun, J. J. Biendicho, L. Balcells, X. L. Fan, J. R. Morante, J. Y. Zhou and A. Cabot, *Angew. Chem., Int. Ed.*, 2022, **61**, e202211570.
- 148 C. H. Li, J. Yu, D. W. Yang, H. Li, Y. P. Cheng, Y. C. Ren, X. Y. Bi, J. C. Ma, R. R. Zhao, Y. T. Zhou, J. Wang, C. Huang, J. S. Li, I. Pinto-Huguet, J. Arbiol, H. N. Zhang, S. Xin and A. Cabot, *J. Am. Chem. Soc.*, 2025, **147**, 8250–8259.
- 149 G. B. Yu, X. Y. Liu, W. Y. Huang, S. X. Wang, J. Q. Zhan, L. Ma, H. P. Li, X. J. Lin, T. C. Liu, K. Amine and H. S. Li, *Adv. Mater.*, 2025, **37**, 2418784.
- 150 X. Y. Liu, X. J. Liu, J. Q. Zhan, W. Yuan, Y. Zhu, W. Y. Huang, H. P. Li, T. C. Liu, K. Amine, H. S. Li and G. H. Yu, *Angew. Chem., Int. Ed.*, 2025, **64**, e202503835.
- 151 T. Yang, Z. Cai, Z. Huang, W. Tang, R. Shi, A. Godfrey, H. Liu, Y. Lin, C.-W. Nan and M. Ye, *Phys. Rev. B*, 2024, **110**, 064427.
- 152 W. Zhong, Y. Qiu, H. Shen, X. Wang, J. Yuan, C. Jia, S. Bi and J. Jiang, *J. Am. Chem. Soc.*, 2021, **143**, 4405–4413.

